MACHANISTIC ANALYSIS OF SODIATION OF ELECTRODES

by

Akshay Biniwale

A Thesis

Submitted to the Faculty of Purdue University

In Partial Fulfillment of the Requirements for the degree of

Master of Science in Mechanical Engineering

School of Mechanical Engineering

West Lafayette, Indiana

December 2019

THE PURDUE UNIVERSITY GRADUATE SCHOOL
STATEMENT OF COMMITTEE APPROVAL

Dr. Partha P. Mukherjee, Chair

School of Mechanical Engineering

Dr. Kejie Zhao

School of Mechanical Engineering

Dr. Luciano Castillo

School of Mechanical Engineering

Approved by:

Dr. Nicole Key

To John B. Goodenough, M. Stanley Whittingham and Akira Yoshino

ACKNOWLEDGMENTS

I would like to thank Dr Partha Mukherjee for giving me an opportunity to work in the group and for his guidance throughout my master's program at Purdue. I would like to thank Dr Kejie Zhao and Dr Luciano Castillo for their insights and willing to serve on my committee.

A special thanks to my research mentor, Ankit Verma for his constant support and advice over the last two years. I would also like to thank Anjul Vyas, Tanay Adhikary and other members of the Energy and Transport Sciences Laboratory for their valuable inputs to this work.

I would also like to thank my family for supporting me throughout my life.

TABLE OF CONTENTS

LIST OF TABLES 7
LIST OF FIGURES 8
ABSTRACT 9
1. INTRODUCTION 10
1.1 Electrochemical Energy Storage 11
1.2 Lithium Ion Batteries 12
1.3 Sodium Ion Batteries 14
2. LITERATURE REVIEW 15
2.1 Sodium Ion Batteries 15
2.1.1 Limitations of Lithium Ion Batteries 15
2.1.2 Properties of Sodium 16
2.1.3 Electrode Materials 18
Carbon Based Negative Electrodes 19
Alloy Based (p - block) Negative Electrodes 19
Alloying vs Intercalation Process 20
2.1.4 Tin based negative electrodes 23
Metallic Tin 23
Tin Phosphide 24
2.2 Modeling Methodologies 24
2.2.1 Macroscopic Model 25
2.2.2 Single Particle Model 28
2.2.3 Mechanical Degradation of Electrodes 29
2.2.4 Modeling of Sodium Ion Batteries 30
3. METHODOLOGY 31
3.1 Single Particle Model 31
3.1.1 Model Development 31
Solid Phase Diffusion 31
Electrode Kinetics 32
3.1.2 Volume Expansion Effects 33

3.1.3 Squeezing Effect 36
3.2 Morphology changes 38
Nano-rods 38
3.3 Finite Volume Formulation 39
Grid Generation 39
Discretizing the governing equation 40
Node 1: Closest to r = 0 41
Node 'N': Closest to r = R_p 42
Solving the set of equations 43
3.4 Material Properties of Tin Phosphide Particles 43
3.5 Material Properties of Tin Particles 45
3.6 Fracture Model 47
4. RESULTS 50
4.1 Validation of Model 50
4.1.1 Tin Phosphide 51
4.1.2 Tin 52
4.2 Effect of changing simulation parameters 54
4.2.1 Particle Size 54
4.2.2 C-rate 55
4.2.3 Reaction rate 56
4.2.4 Cell resistance 57
4.2.5 Diffusivity of sodium 57
4.3 Additional Effects in the Single Particle Model 59
4.4 Morphology Changes 62
4.5 Fracture Model 63
Strain Relaxation 64
5. CONCLUSION AND FUTURE WORK 67
5.1 Conclusion 67
5.2 Future Work 68
REFERENCES 69

LIST OF TABLES

Table 2.1. Comparison of properties of Lithium and Sodium [4] 17
Table 3.1. Properties used as inputs in the Single Particle Model for Sn_4P_3. 44
Table 3.2. Properties used as inputs in the Single Particle Model for tin. 46
Table 4.1. Parameter values for Sn_4P_3 used in this study. 52
Table 4.2. Parameter values for Sn used in this study. 53
Table 4.3. Parameter values for the squeezing effect used for Sn_4P_3 simulations. 62
Table 4.4. Cell capacity for different particle morphologies and charge rates. 62
Table 4.5. Material properties used in the fracture model. 63
Table 4.6. Effect of strain rate on the number of broken bonds. 64

LIST OF FIGURES

Figure 1.1. Renewable energy share of global energy consumption [2]. 10
Figure 1.2. US greenhouse gas consumption by sector [3]..... 11
Figure 1.3. Energy density vs specific density for different batteries [5]..... 12
Figure 1.4. Schematic of a lithium ion battery [12]..... 13
Figure 2.1. Predicted lithium demand and availability over the 21st century [14]..... 16
Figure 2.2. Change in price and production of Li_2CO_3 between 1990 and 2010 [15] 17
Figure 2.3. Representation of abundance of elements in Earth's crust [2] 18
Figure 2.4. Representation of different mechanisms for charge insertion in electrodes [25]..... 20
Figure 2.5. Voltage vs discharge capacity of anode materials for NIBs. [2] 21
Figure 2.6. Cycle life vs storage capacity of anode materials for NIBs [2]..... 22
Figure 2.7. Stepwise sodiation of tin particles [27] 24
Figure 2.8. Overview of models of electronic systems [56] 25
Figure 2.9. Representation of a cell in each modelling technique [56]. 26
Figure 2.10. Decreasing order of complexity in macroscopic models [56]..... 27
Figure 3.1. Representation of a FVM grid..... 40
Figure 4.1. Comparison of simulation and experimental results for Sn_4P_3 51
Figure 4.2. Comparison of simulation and experimental results for Sn. 53
Figure 4.3. Effect of changing particle size on the electrode performance. 54
Figure 4.4. Effect of changing C-rate on the electrode performance..... 55
Figure 4.5. Effect of changing reaction rate on the electrode performance..... 56
Figure 4.6. Effect of changing electrolyte resistance on cell performance..... 57
Figure 4.7. Effect of changing diffusivity on cell performance..... 58
Figure 4.8. State of charge along particle radius for different diffusivity values. 58
Figure 4.9. Simulation and experimental results for Sn_4P_3 with the squeezing effect..... 60
Figure 4.10. Simulation and experimental results for Sn_4P_3 without the squeezing effect. 61
Figure 4.11. Microcrack formation on particles at different C-rates 66

ABSTRACT

The single particle model was extended to include electrode and particle volume expansion effects observed in high capacity alloying electrodes. The model was used to predict voltage profiles in sodium ion batteries with tin and tin-phosphide negative electrodes. It was seen that the profiles predicted by the modified model were significantly better than the classical model. A parametric study was done to understand the impact of properties such as particle radius, diffusivity, reaction rate etc on the performance of the electrode. The model was also modified for incorporating particles having a cylindrical morphology. For the same material properties, it was seen that cylindrical particles outperform spherical particles for large L/R values in the cylinder due to the diffusion limitations at low L/R ratios. A lattice spring-based degradation model was used to observe crack formation and creep relaxation within the particle. It was observed that the fraction of broken bonds increases with an increase in strain rate. At low strain rates, it was seen that there was a significant expansion in particle volumes due to creep deformation. This expansion helped release particle stresses subsequently reducing the amount of fracture.

1. INTRODUCTION

In April 2016, 195 countries signed the United Nations Paris agreement with the aim to reduce the global average temperature to 2 degrees higher than pre-industrial levels [1]. The strategy to reach this target involved increasing the use of renewables by 20% and reducing CO2 emissions by 20%. These goals can only be achieved through technological innovation.

In 2018, only 15% of the total energy consumed in the United States came from renewables [2]. The energy that can be harnessed from renewables can, in theory, satisfy all of earth's energy requirements. The biggest problem with renewables is the fluctuation of energy available for use. For instance, solar energy is available for only a few hours every day. To ensure that energy generated from renewables is available everywhere and throughout the year, it is important to develop energy storage devices.

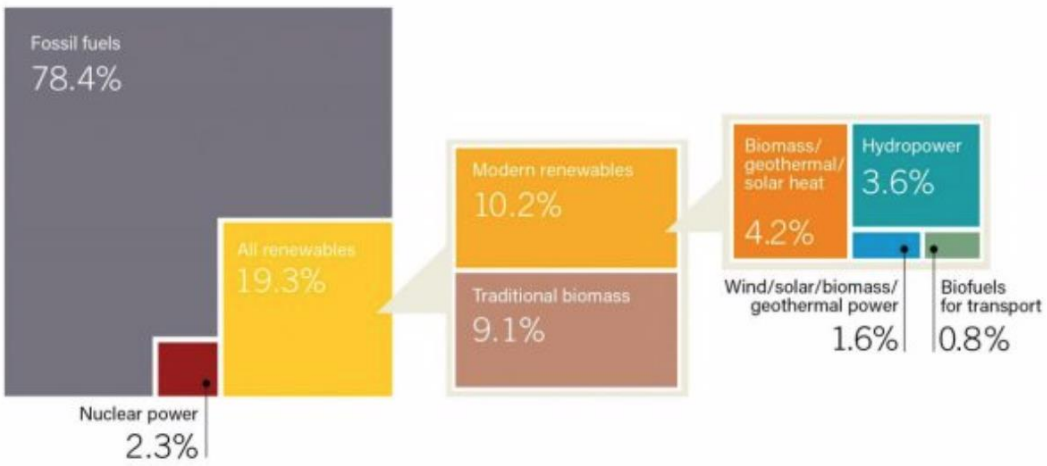

Figure 1.1. Renewable energy share of global energy consumption [2].

The Environmental Protection Agency (EPA) has found that 29% of total greenhouse gases in the United States come from transportation [3]. To decrease this emission, there needs to be a shift from conventional gasoline and diesel vehicles to fully electric and hybrid vehicle. The limiting factor in the widespread adoption of electric vehicles is the limited range of the current energy storage technology.

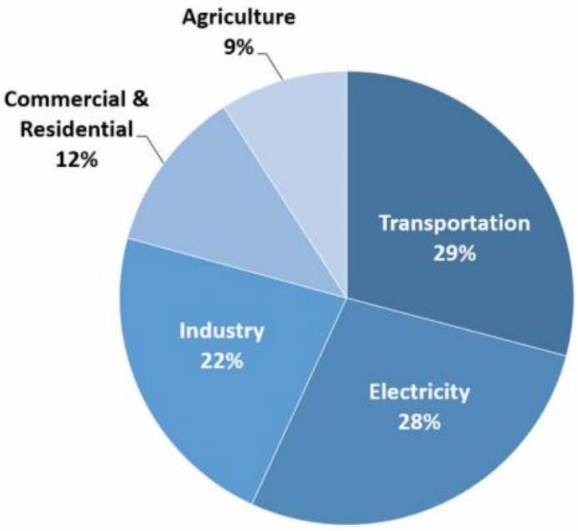

Figure 1.2. US greenhouse gas consumption by sector [3].

Hence, we see that development and improvement of energy storage devices can help in achieving both the goals laid out by the Paris agreement. Of all the energy storage devices, the most crucial ones are electrochemical storage devices or batteries due to their very high energy densities and potential for widespread application.

1.1 Electrochemical Energy Storage

An electrochemical device is a device which generated energy, in the form of electricity, due to a chemical reaction taking place in the device. The first 'battery' was built by Alessandro Volta and Luigi Galvani in the 1700s. This system was a pile of alternating zinc and silver disks separated by a cloth dipped in a NaCl solution [4].

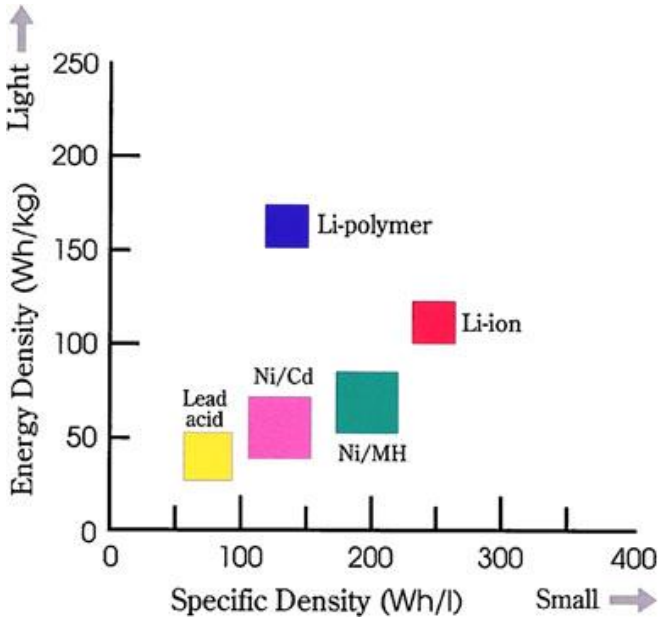

Figure 1.3. Energy density vs specific density for different batteries [5].

Leclanche built a battery in 1866 using a zinc rod and a manganese oxide-carbon mixture in an aqueous ammonium chloride solution [6]. This was followed by the introduction of the lead acid battery rechargeable battery in 1859 and the nickel cadmium battery in 1901.

The biggest problem with these devices was the low energy density of the batteries. This changed in the 1950s when lithium was discovered as a material for making batteries. The lithium-iodine battery, developed in 1972, had an energy density five times that of a zinc - mercury oxide battery.

Today, lithium ion batteries are used everywhere from small electronic devices to batteries of electric vehicles.

1.2 Lithium Ion Batteries

Lithium is the lightest metal in the periodic table. It also has the highest energy density and highest voltage making it an ideal candidate for electrochemical storage.

The first study of lithium ion batteries was done by Harris in 1958 [7]. Lithium ion technology became more popular in the 1970s when the first primary cells were commercialised. One of the important breakthroughs was the discovery of intercalation electrodes [8]. These electrodes had open structures and hence were reversibly capable of accepting and releasing lithium ions. The sudden interest in batteries was due to the growth of the consumer electronics market [5]. In the 1980s, development of rechargeable batteries took place. Exxon and Moli attempted to commercialize the Li/TiS_2 and Li/MoS_2 systems respectively [9].

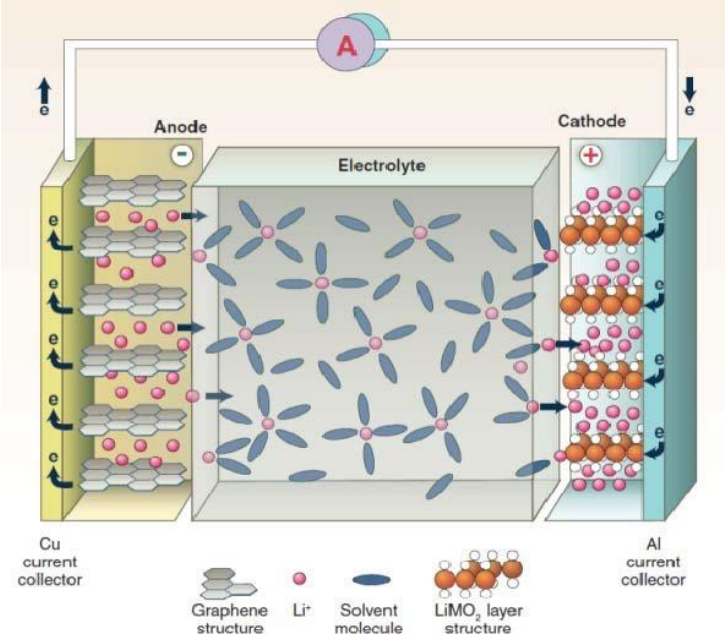

Figure 1.4. Schematic of a lithium ion battery [12].

During this time, lithium metal was used as the anode in the cell. It was observed that metallic lithium interacted with the electrolyte which led to certain safety issues with the cell. Following this, a number of different anode materials were tested in the cell. The next breakthrough in lithium ion cells was the development of a system known as the lithium rocking chair battery [10]. The system involved using two insertion electrodes - one capable of accepting lithium ions and the other capable of releasing lithium ions.

Development of this system identified graphite as a suitable anode material and lithium cobalt oxide as a suitable cathode material. Sony first commercialized these batteries in 1991 [11]. Since, researchers have identified a number of cathode and anode material suitable for use in lithium ion batteries. However, the electrodes materials used by Sony in 1991 are still commonly used in modern lithium ion batteries.

1.3 Sodium Ion Batteries

It is predicted that the demand for lithium will exceed the availability of lithium in the earth's crust. This has motivated researchers to look for alternate technologies for electrochemical energy storage.

Sodium, also being an alkali metal, has properties very similar to that of lithium. In addition, it is low cost, widely available and has good electrochemical properties making it an ideal candidate to use instead of lithium.

In the next chapter, an extensive literature review is presented to understand the newest developments in sodium ion batteries. This review will help to identify appropriate electrode materials, understand the performance and ultimately build a physics-based model to predict the performance of sodium ion batteries.

2. LITERATURE REVIEW

2.1 Sodium Ion Batteries

Sodium ion batteries (NIBs) were first investigated alongside lithium ion batteries (LIBs) in the 1970s [17-23]. However, researchers focused on development of LIBs due to 2 reasons [16] –

1. LIBs provided a higher energy density as compared to NIBs.
2. There were no suitable materials discovered that could be used for negative electrodes in NIBs.

In 2000, Stevens and Dahn [24] reversibly inserted sodium into a hard carbon electrode to achieve a reversible capacity of 300 mAh/g. This was the turning point for research in NIBs.

The next few sections describe the limitations of lithium ion batteries and why sodium is a good alternative. Then, a set of good electrode material are identified for sodium ion batteries.

2.1.1 Limitations of Lithium Ion Batteries

Lithium Ion batteries have been studied for a very long time. As the automotive industry moves towards electric vehicles, the demand for lithium will significantly increase. The Research Center for Energy Economics predict that the demand for lithium could surpass the availability by 2100 (Figure 2.1). As the demand increases, the price will also increase. Figure 2.2 illustrates the fluctuation of the price of Li_2CO_3 between 1990 and 2010. As the demand for lithium batteries grew in the 21st century, there was a sharp rise in the price of Li_2CO_3.

Due to the concerns regarding the cost and availability of LIBs, researchers began looking at alternative materials for building batteries. Sodium is an important candidate due to its similarity to lithium.

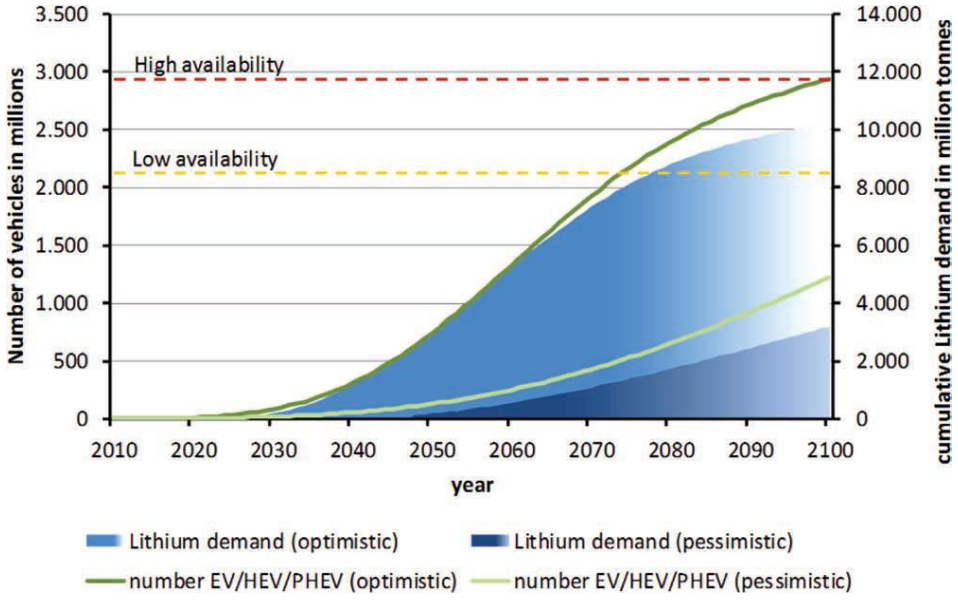

Figure 2.1. Predicted lithium demand and availability over the 21st century [25]

2.1.2 Properties of Sodium

Sodium and lithium, are both highly reactive alkali metals with only one electron in the valence shell. Both of them easily lose the electron to form a positively charged ion. The reduction potentials of the two are also very similar.

Since, sodium and lithium have similar chemical properties (table 2.1), the fundamental principles of sodium-ion batteries and lithium ion batteries are identical [13]. Sodium is also more abundant (as seen in figure 2.1) and significantly cheaper than lithium.

Sodium-ion batteries have lower energy densities than lithium ion batteries. Hence, they cannot replace LIBs in applications where using larger batteries is not feasible. However, they are good candidates for applications where energy density is not too important such as electric buses and stationary storage [13].

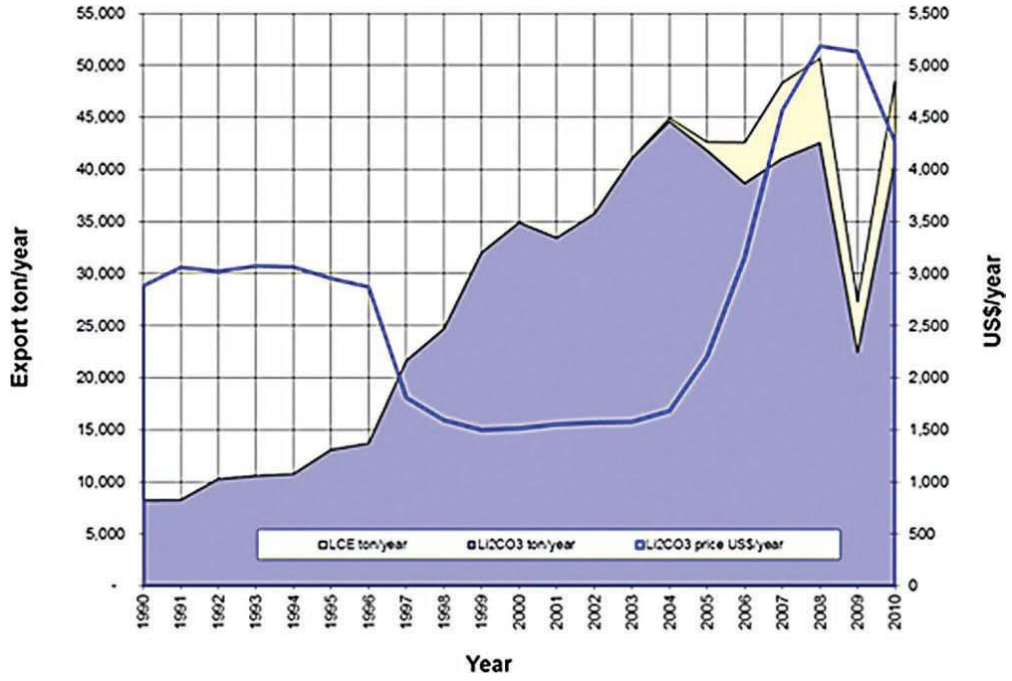

Figure 2.2. Change in price and production of Li_2CO_3 between 1990 and 2010 [26]

Table 2.1. Comparison of properties of Lithium and Sodium [16]

	Li^+	**Na^+**
Relative atomic mass	6.94	23.00
Ionic radii (A)	0.76	1.02
E° (vs SHE) (V)	-3.04	-2.71
Melting point ($^\circ$C)	180.5	97.7
Theoretical capacity of metal electrode (mAh/g)	3861	1166
Coordination preference	Octahedral and tetrahedral	Octahedral and prismatic

Based on these similarities, it is clear that NIBs provide a good alternative to LIBs [13, 15].

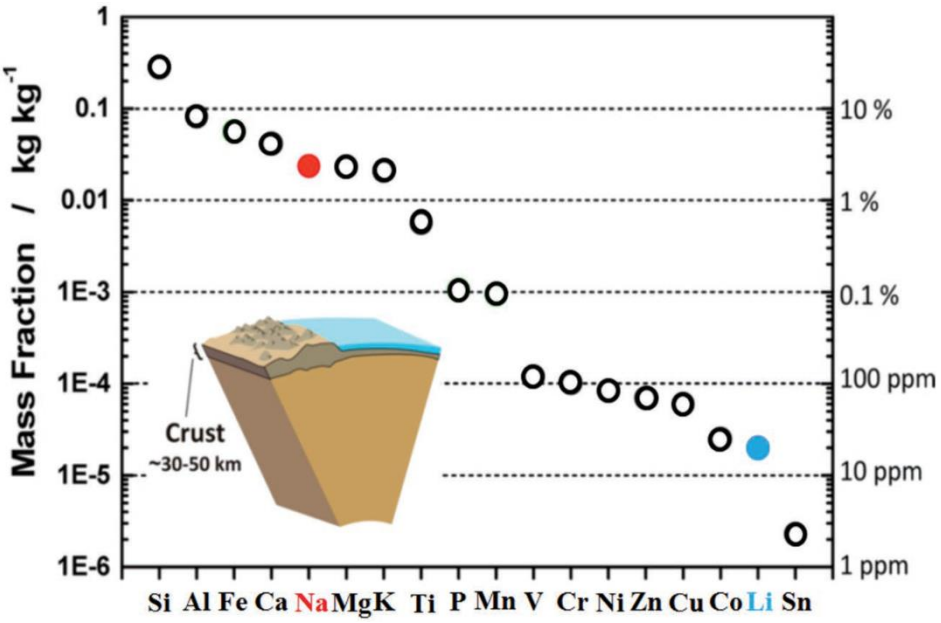

Figure 2.3. Representation of abundance of elements in Earth's crust [14]

2.1.3 Electrode Materials

Sodium ion battery research began by attempting to use materials previously used for lithium ion batteries. Researchers have used materials such as Na_2FePO_4F [26] and $NaMO_2$ (M = V, Cr, Mn, Fe) structures with NIBs. However, it was found that there was almost no discharge capacity after the first cycle [27-33].

Chevrier and Ceder compared the volumetric energy densities of lithium and sodium in commonly used LIB negative electrodes [36]. They found that the energy densities for sodium are significantly less for lithium.

There are four kinds of material used as negative electrodes for NIBs [16]-

1. Carbon based materials
2. Polyanion compounds / oxides
3. P-block elements
4. Oxides/sulphides with conversion reaction

Of the four, carbonaceous materials and p-block materials are most important and hence will be discussed in detail.

Carbon Based Negative Electrodes

In 1993, Doeff et al were able to achieve a large reversible capacity by inserting Na-ions into petroleum coke [44]. After that, Stevens and Dahn reported the reversibility of Na ion in hard carbon [24] in 2000. Following this, a lot of researchers have attempted to study and develop carbon-based materials for sodium ion batteries [44-52].

Graphite is one of the most popular negative electrode materials in LIBs. However, it cannot be used for NIBs as sodium ions cannot intercalate between carbon sheets [23-24, 34]. After further investigations, researchers found that the low capacity in graphite is due to thermodynamic effects, specifically due to the competition between ionization energy and enthalpy of ion substrate bonding [53].

Hard carbon has a good gravimetric capacity and a good cyclability. However, the performance of hard carbon depends on solvents, electrolyte salts, additives and binders [16] and needs further investigation.

Alloy Based (p - block) Negative Electrodes

Alloys of lithium such as Li-Sn and Li-Si have significantly higher reversible capacity as compared to Li-graphite and hence have been extensively investigated [22, 54-56]. Similarly, researchers have investigated Sn, Ge, P and Sb based materials for NIBs [40-43]. It was seen that NIBs have lower energy densities with alloy-based materials as compared to LIBs [36].

These materials have shown high first cycle electrode capacities and low electrode potentials with sodium. Sodiation of these materials causes very large volume expansions - 520% for Sn, 126% for Ge, 300% for P and 390% for Sb electrodes [40-43]. This volume expansion can cause loss of electric contact and is hence an important concern for these electrodes. These materials are also

good candidates for large scale energy storage because they are environment friendly and low cost [14].

Alloying vs Intercalation Process

Palacin represented the structural changes in three charge insertion mechanisms - intercalation, alloying and conversion in an illustrative figure [35]. While this was originally made for LIBs, it can also be used to represent NIBs.

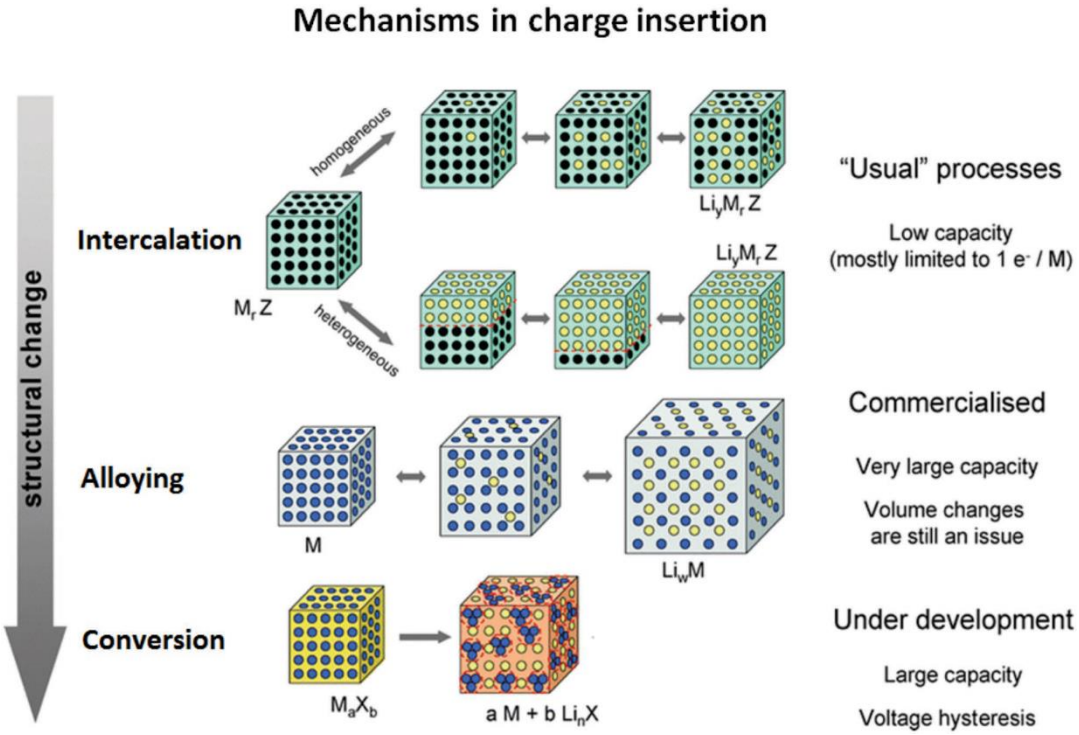

Figure 2.4. Representation of different mechanisms for charge insertion in electrodes [35].

In intercalation processes, the host matrix retains its structural integrity after an insertion / deinsertion process [14]. An instance of this process is the inter-layer insertion of sodium in crystalline compounds. There is almost no volume change in this process. Carbon based materials insert charge through the intercalation process.

The process of alloying is represented in equation 2.1. There is a significant volume change in the host matrix upon the insertion of sodium. This volume change can lead to pulverization, particle disconnection and isolation of active materials [38]. It is important to come up with strategies that can prevent this from happening.

$$Na^+ + M + xe^- \leftrightarrow Na_xM \qquad (2.1)$$

The third kind of reactions, conversion reactions, have large volume expansions and high hysteresis leading to low energy efficiency [39]. Hence, they will not be discussed further.

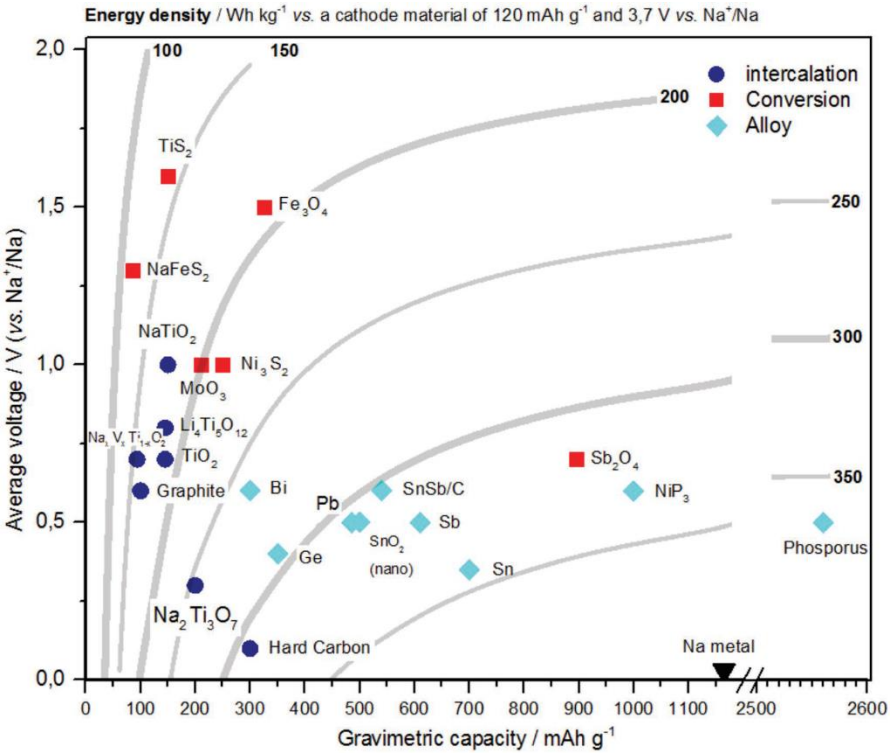

Figure 2.5. Voltage vs discharge capacity of anode materials for NIBs. [14]

The performance of a material depends on the average voltage, discharge capacity and cyclability of the electrode. An ideal material would have a low anodic potential, high capacity and high cyclability.

As seen in figure 2.5, intercalation materials have low electrode potential values but low gravimetric capacities. On the other hand, alloy electrodes are seen to have a higher capacity compared to intercalation. They also have higher energy densities compared to intercalation-based materials. However, there is a large volume expansion in these materials leading to a low cyclability of the system.

Metallic sodium, which seems to be the best candidate in figure 2.5, has a lot of issues such as dendrite formation and unstable SEI formation [15]. Due to these practical considerations, it cannot be used as an anode material.

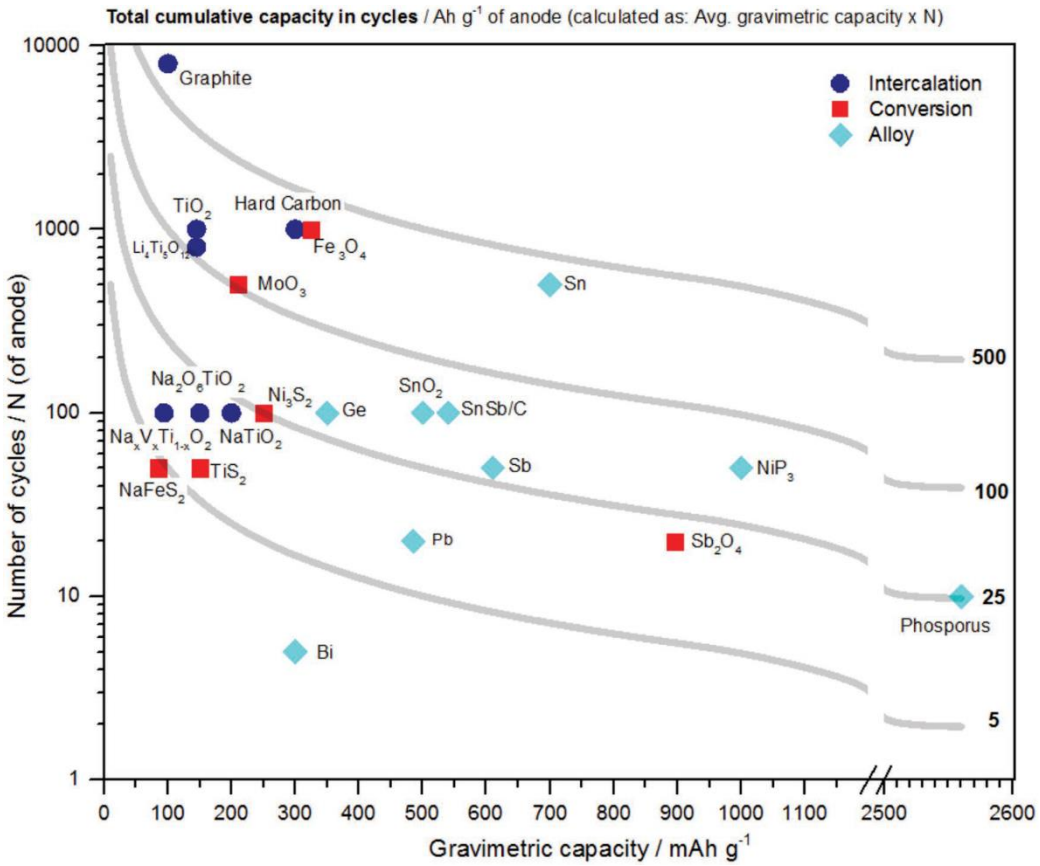

Figure 2.6. Cycle life vs storage capacity of anode materials for NIBs [14].

It is seen in figure 2.6 that alloy materials have significantly higher cyclability than intercalation materials. Considering both, the storage capacity and number of cycles, tin based electrodes appear to be ideal candidates for negative electrodes.

2.1.4 Tin based negative electrodes

Tin has a high charge storage capacity by volume and weight [57]. The theoretical capacity of tin (847 mAh/g) is double that of graphite. Tin is also non-toxic, abundant and safe to work with [58] making it a good candidate for electrodes.

The most common tin based materials for sodiation are - Metallic tin, tin oxide, tin sulphide and tin phosphide. Of these materials, only metallic tin and tin phosphide will be discussed in detail.

Metallic Tin

Sodium and metallic tin form the following phases [36] – $NaSn_6$, $NaSn_4$, $NaSn_3$, $NaSn_2$, Na_9Sn_4, Na_3Sn, $Na_{15}Sn_4$. The sodiation process has 4 monotonically decreasing plateaus in the voltage - capacity plot indicating two phase processes [36, 37, 57]. A large hysteresis was frequently observed in this process [63].

A number of investigations have been done to understand the mechanism of sodiation in tin. Obrovac et al [37] studied the reaction sequence of sodiation using X-ray analysis. They were able to achieve the theoretical capacity of 847 mAh/g with a C rate of C/50. In this process, they observed 3 intermediate phases. However, it is unlikely that these will be seen at typical higher C-rates.

Wang et al [59] investigated the insertion of sodium into tin using in situ Transmission Electron Microscopy (TEM). They observed that the sodiation is a two-step reaction with the following steps (Figure 2.7) –

1. Formation of an amorphous Na_xSn with a volume expansion of 60 %.
2. Na - rich crystalline $Na_{15}Sn_4$ phase with a volume expansion of 420 %.

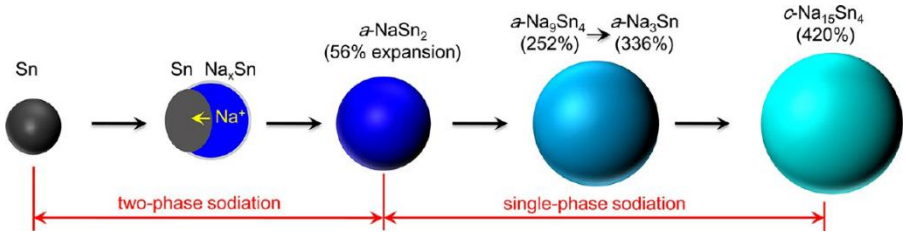

Figure 2.7. Stepwise sodiation of tin particles [37]

Tin Phosphide

Tin phosphide is a promising material due to its high theoretical capacity of 1132 mAh/g [60-62]. A majority of the capacity is in the useful range, i.e. below 0.5 V vs Na/Na^+.

$$Sn_4P_3 + 24Na^+ + 24e^- \leftrightarrow Na_{15}Sn_4 + 3Na_3P \qquad (2.1)$$

In a study done by Qian et al [61], it was seen that a maximum reversible capacity of 850 mAh/g was obtained. The proposed reaction is given in equation 2.1. It was also seen that the phosphorus prevents agglomeration of tin. It was also seen that Sn_4P_3 phase does not form after desodiation.

2.2 Modeling Methodologies

Computational modeling is being used in modelling of lithium ion batteries for a long time. In addition to saving time, modeling can also be used to verify experimental hypothesis and provide guidelines for improving materials [63].

The first instance of macroscopic battery modelling was seen in the 1970s to model fuel - cell sandwich models. These models were capable of modelling complex processes due to the construction of different regions within the cell [63]. The operation of a Li-water system was modeled by the Bennion Research in 1976 [64]. Then, Newman's group simulated the transient discharge process of a lead acid battery in 1979 [65]. In the next 10-15 years, a number of groups began using similar models.

Modeling of lithium ion batteries ranges from vehicle and battery pack level system simulations to electronic structure simulations to simulate atomistic structures [66]. An overview of modelling

of modelling techniques is given in Figure 2.8. Since this work consists of continuum level simulations, only the macroscopic model will be explained in detail.

2.2.1 Macroscopic Model

The continuum scale formulation of lithium ion batteries involves the use of mesoscopic or macroscopic models to predict battery performance. This is one of the most popular modeling techniques and also be used for prediction of battery life [66].

Macroscopic models solve the following equations for the cell -

1. Conservation of charge - to ensure that no charge is generated or consumed in each phase.
2. Conservation of species - to account for the transport of active material in each phase.
3. Conservation of energy - to study heat generation and temperature evolution in the cell.
4. Electrode kinetics - given by the Butler Volmer reaction at the interface of the electrode and electrolyte.

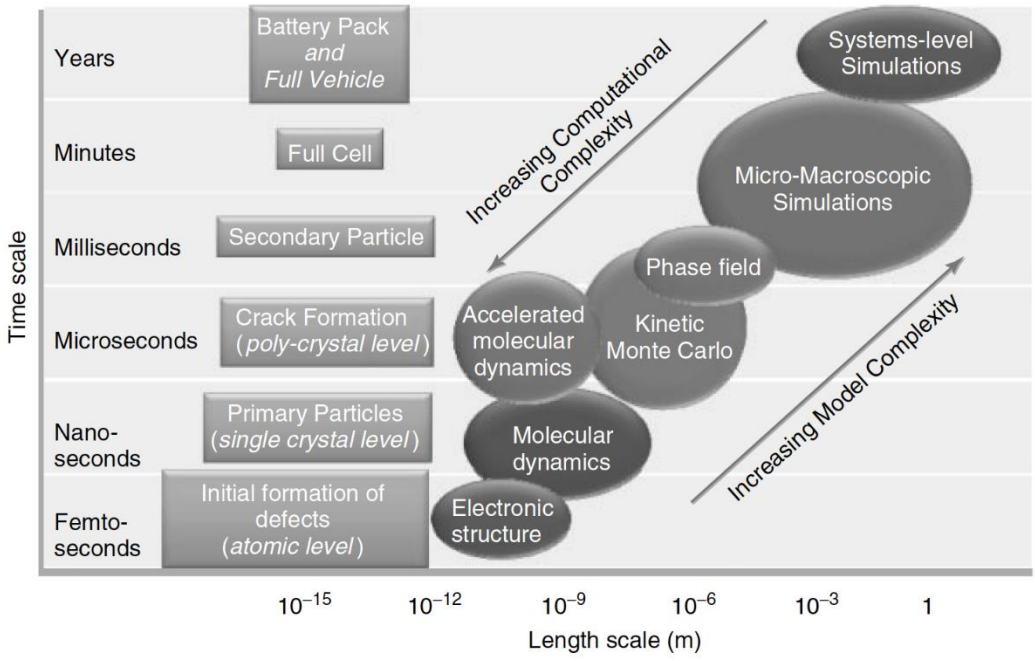

Figure 2.8. Overview of models of electronic systems [66]

Figure 2.9 gives an overview of common macroscopic modelling techniques and the representation of a cell in each of those approaches.

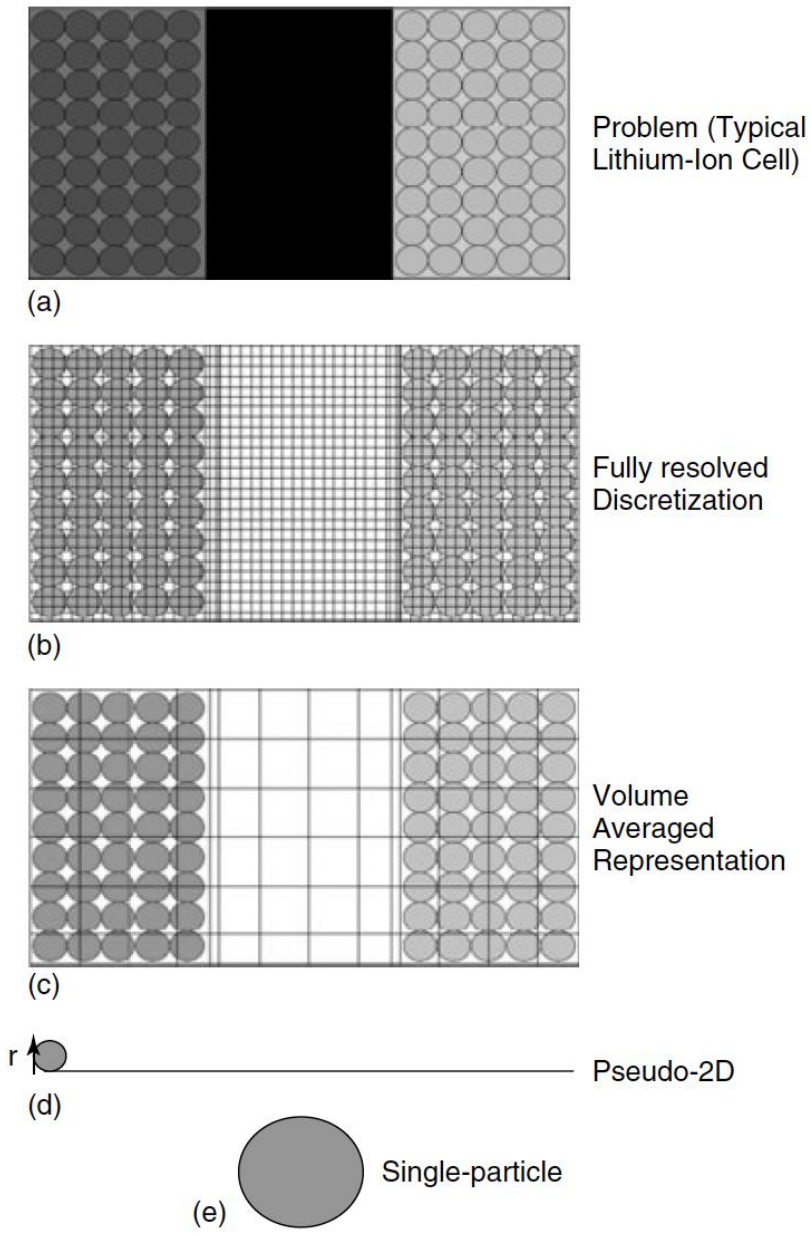

Figure 2.9. Representation of a cell in each modelling technique [56].

Figure 2.10 represents the decreasing order of complexity of these approaches. The techniques, as given in Mukherjee et al [66] are as follows –

1. Direct Numerical Simulation (DNS) - In this technique, all the components in the battery - electrodes, electrolyte binder etc. - are completely resolved. This is computationally the most intensive technique (Figure 3.2b).
2. Volume Averaged Formulation - In this approach, all the quantities of interest - diffusion, charge etc. - are average across a representative volume to simplify the computation. (Figure 2.9c). The interfacial processes are also average in this approach.
3. Pseudo 2D model - This technique, developed by Fuller, Doyle and Newman [67,68], treats the battery components - the electrodes and separator - as a series of identical spherical particles. Transport in each of the particles is given by radial diffusion [69]. The solution phase properties are assumed to vary in only one direction (Figure 2.9d).
4. Single Particle model - In this approach, the entire electrode is treated as a lumped single spherical particle (Figure 2.9e). It is assumed that there are no transport limitations due to the electrolyte phase and hence electrolyte transport is not solved. Details of this model are discussed in Chapter 3 of this thesis.

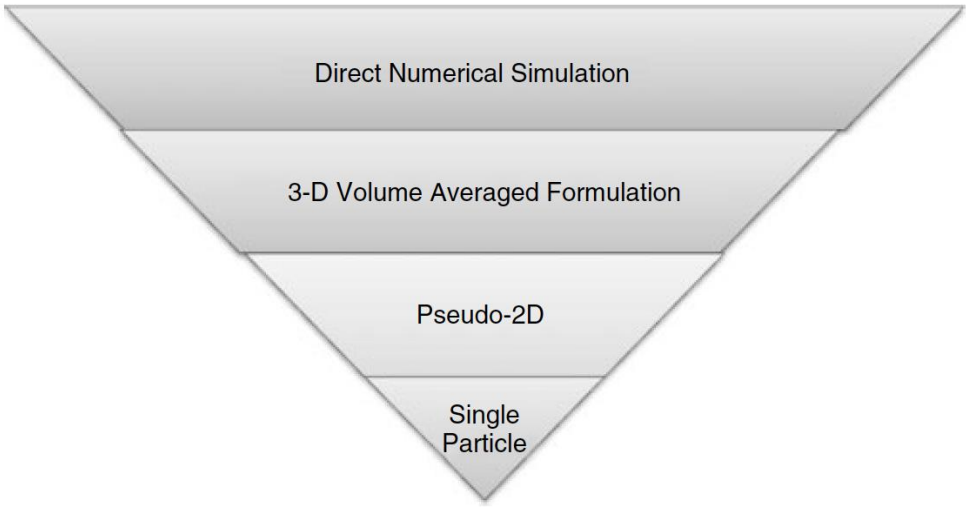

Figure 2.10. Decreasing order of complexity in macroscopic models [66]

While all of these models were originally developed for lithium ion batteries, due to the similarity in the electrochemistry of sodium and lithium, these models can also be used for modeling sodium ion batteries.

2.2.2 Single Particle Model

The Single Particle model is a simplified model where the electrode is treated as a single spherical particle. The surface area of the particle is equal to the total active area of the electrode. The model assumes that there are no transport limitations due to the electrolyte phase [69]. Hence it ignores the distribution of concentration and potential in the electrolyte phase [72].

The Single Particle Model (SP model), introduced by Haran et al, was first used in 1998 for simulating the performance of metal hydrides [67]. In 2004, Ning and Popov used the model to simulate capacity fade for lithium ion batteries [68].

Santhanagopalan et al [69] compared the performance of the SP model to the Pseudo 2D model (P2D model) and the Pseudo 2D model with parabolic approximation (PP model). They observed that the SP model is orders of magnitude faster than the other models and can successfully simulate the cycling for charge rates less than 1 C. At rates greater than 1 C, concentration gradients in the electrolyte phase are the major factor in limiting species transport. Thus, the SP model is not very accurate at such high charge rates.

Guo et al extended the single particle model by adding an energy balance equation [72]. Then observed good agreement between this extended model and the PP thermal model.

Chandrasekharan et al applied the single particle formulation to a Li-Si system [73]. They extended the model to account for the 280% [74] volume expansion of the particle.

2.2.3 Mechanical Degradation of Electrodes

Commercially available lithium ion batteries use materials such as graphite for the negative electrode and lithium cobalt oxide or lithium manganese oxide as positive electrode materials. In the intercalation and deintercalation of lithium into these materials, the volume expansion is low. Hence the strain generated in the particles is also small [75,76].

When high specific capacity materials or alloying anode materials such as silicon and tin are used as intercalation electrodes, they experience a very large volume expansion causing mechanical failure [77] and eventual capacity fade [78].

A number of researchers have attempted to investigate the relationship between this capacity fade and a set of cell parameters such as particle size, temperature, strain rate and charge rate [79-80]. It was observed that micron sized alloying materials (Si, Sn and Ge) experience fracture irrespective of the material [80-83]. However, in nanosized particles, different observations were made. Nanosized silicon particles were seen to have surface cracks due to anisotropic expansion [81]. Lithiated germanium had no cracks possibly due to the isotropic expansion of active material [84]. Tin particles of size 300-500 nm did not experience any fracture during lithiation [85]. Clearly, understanding the underlying mechanism of microcrack formation is important to predict capacity fade in the electrode.

Tin, an ideal electrode material for sodiation, was observed to be heavily influenced by creep deformation [86, 87]. The microcrack formation in tin was seen to occur through two mechanisms [88] –

- At the two-phase interface - through concentration gradient induced stresses.
- At the active material particle surface - due to high expansion induced stresses.

It was also observed that there is no significant crack formation occurs at low rates of operation [78] due to creep relaxation effects. Barai et al developed a computational model to capture this reduced mechanical degradation due to creep relaxation for lithiated tin particles [88].

In this thesis, the model developed by Barai et al has been used to observe mechanical degradation in sodiated tin particles.

2.2.4 Modeling of Sodium Ion Batteries

The goal of this thesis is to develop a model for sodium ion batteries with tin based electrodes. In such an alloying process, a large volume expansion is expected.

Due to the similarity in lithium and sodium chemistries, models used for modeling lithium ion batteries can be applied to model the performance of sodium ion batteries.

In this work, the single particle model extended by Chandrasekharan et al [73] has been modified and used to predict the performance. It was then validated using experimental results for metallic tin and tin phosphide.

3. METHODOLOGY

3.1 Single Particle Model

3.1.1 Model Development

The Single Particle Model [69, 72, 76, 89] has been used to predict the cycling performance of batteries in this work. The Single Particle model is a simplified model where the electrode is treated as a single spherical particle. The surface area of the particle is equal to the total active area of the electrode. The concentration gradient in the electrolyte phase is neglected. The particle to particle contact resistance is also ignored in this model.

Solid Phase Diffusion

Diffusion in the solid phase is given by Fick's Law in the spherical coordinate system [89] as shown in Equation 3.2.1.

$$\frac{\partial c_j}{\partial t} = \frac{D_j}{r^2}\frac{\partial}{\partial r}\left(r^2\frac{\partial c_j}{\partial r}\right) \tag{3.1.1}$$

Here c_j the concentration of sodium in the sphere and the subscript j represents the positive / negative electrode. D_j the solid phase diffusion coefficient. Due to symmetry of the particle, there is no flux at the center of the particle (Eqn 3.1.2). The particle also has a constant molar flux of sodium ions at the surface (Eqn 3.1.3). The initial concentration in the electrodes serves as the initial condition (Eqn 3.1.4).

$$\left(D_j\frac{\partial c_j}{\partial r}\right)_{r=0} = 0 \tag{3.1.2}$$

$$\left(D_j\frac{\partial c_j}{\partial r}\right)_{r=R_j} = -J_j = -\frac{i}{n_e F} \tag{3.1.3}$$

$$c_j(t=0) = c_{ini,j} \tag{3.1.4}$$

R_j the particle radius, i represents the current density, n_e represents the number of electrons participating in the reaction and F the Faraday constant. The molar flux of sodium ions J_j is directly related to the current I passing through the cell tabs as shown in equation 3.1.5.

$$J_p = \frac{I}{FS_p} \qquad J_n = \frac{-I}{FS_n} \tag{3.1.5}$$

S_j represents the total electroactive area of the electrode. The electroactive area is also related to the volume fraction j, electrode volume V and particle radius R_j in equation 3.1.6.

$$S_j = \frac{3\varepsilon_j V_j}{R_p} \tag{3.1.6}$$

Equation 6 is used when accounting for a multiple particle system. If a single particle is used instead of multiple particles, then the electroactive area is given by equation 3.1.7.

$$S_j = 4\,\pi\,R_p^2 \tag{3.1.7}$$

Electrode Kinetics

The electrochemical reaction in a sodium tin system is given by equation 3.1.8.

$$Sn + 3.75\,Na^+ + 3.75\,e^- \leftrightarrow Na_{3.75}Sn \tag{3.1.8}$$

The reaction kinetics at the surface of the particle are defined by the Butler Volmer reaction (equation 3.1.9). Symmetric anodic and cathodic transfer coefficients of value 0.5 have been assumed.

$$FJ_j = i_o\left[e^{\frac{0.5F\eta_j}{RT}} - e^{\frac{-0.5F\eta_j}{RT}}\right] \tag{3.1.9}$$

In this equation, i_o is the exchange current density, R is the universal gas constant, T is the temperature and η_j the overpotential. The exchange current density is the current density at the Open Circuit Potential (OCP). The exchange current density is a function of the maximum concentration of sodium ions in tin c_{max} and the surface concentration c_{surf} as expressed in equation 3.1.10.

$$i_o = Fkc_e^{0.5}\left(c_{max} - c_{surf}\right)^{0.5} c_{surf}^{0.5} \quad (3.1.10)$$

The rate constant of the electrochemical reaction at the electrode is given by k. The overpotential j is defined in equation 3.1.11.

$$\eta_j = \phi_{1,j} - \phi_{2,j} - U_j \quad (3.1.11)$$

In this equation, $\phi_{1,j}$ the solid phase potential, $\phi_{2,j}$ is the solution phase resistance and U_j is the Open Circuit Potential (OCP). The OCP is a function of the state of charge (SOC) at the surface of the particle.

The state of charge is a dimensionless measure of the extent to which the particle is charged. It is expressed in terms of c_{max} shown in equation 3.1.12. c_{max} for a cell is calculated from the molecular mass, density and stoichiometry.

$$x_j = \frac{c_j}{c_{j,max}} \quad (3.1.12)$$

The single particle model treats potential drop across the electrolyte as a bulk electrolyte resistance term Rcellas given in equation 3.1.13. The cell voltage is calculated as the difference between the solid phase potentials (Eqn 3.1.14).

$$\phi_{2,p} - \phi_{2,n} = IR \quad (3.1.13)$$

$$V_{cell} = \phi_{1,p} - \phi_{1,n} \quad (3.1.14)$$

3.1.2 Volume Expansion Effects

Chandrasekharan et al [73] used material balance on lithium and reformulated the single particle model to account for volume expansion effects in a lithium-silicon system.

While accounting for the volume expansion, the original governing equations get modified. The current density and concentration get replaced by the normalised current density and concentration values. A detailed derivation of the equations accounting for volume expansion is given in [73].

The following modified equations are obtained -

$$\left(D_j \frac{\partial c_j}{\partial r}\right)_{r=R_j} = -\frac{i'}{n_e F} \tag{3.1.15}$$

$$i_o = F k c_e^{0.5} \left(c_{max} - c'_{surf}\right)^{0.5} {c'_{surf}}^{0.5} \tag{3.1.16}$$

The normalized current density is expressed in equation 3.1.17 and the normalized concentration is given in equation 3.1.18.

$$i' = i \left[\frac{R_{p,o}}{R_p(t)}\right]^3 \tag{3.1.17}$$

$$c'_{surf} = c_{surf} \left[\frac{R_p(t)}{R_{p,o}}\right]^3 \tag{3.1.18}$$

Here R_{po} represents the radius of the particle at time $t = 0$ and $R_p(t)$ represents the radius at any time t after that. $c_{max,o}$ represents the maximum concentration of sodium ions in the particle with respect to the initial, unexpanded volume (equation 3.1.19).

$$c_{max,o} = N_{tot} V_{p,o} \qquad V_{p,o} = \frac{4}{3} \pi R_{p.o}^3 \tag{3.1.19}$$

$V_{p,o}$ represents the initial volume of the particle and N_{tot} represents the total number of moles of sodium that can be inserted into the electrode. N_{tot} can also be expressed in terms of c_{max} (equation 3.1.20).

$$N_{tot} = V_{p,max}\, c_{max} = \frac{4}{3} \lambda\, \pi\, R_{p,o}^3\, c_{max} \tag{3.1.20}$$

λ represents the volume expansion coefficient or the ratio of the maximum expanded volume and the initial unexpanded volume. For the intercalation of sodium in tin, this coefficient is equal to 5.2 [5].

In this case, the particle radius and volume are a function of time. Obravac et al found a relation between the lithiated molar volume for different alloys [74]. Chandrasekharan et al [73] used Obravac's work to find a relation between radius and state of charge during lithiation (equation 3.1.21).

$$\frac{R_p(t)}{R_{p,o}} = \left(1 + \frac{3.75\, V_{Na}\langle x\rangle}{V_{Sn}}\right)^{\frac{1}{3}} \tag{3.1.21}$$

$$R_p(t=0) = R_{p.o}$$

Here, $\langle x\rangle$ is the dimensionless volume average concentration in the entire particle (equation 3.1.22-23). The localized state of charge is given in equation 3.1.24.

$$\langle x\rangle = \frac{\frac{4}{3}\pi\left[R_p(t)\right]^3}{N_{tot}}\langle c\rangle \tag{3.1.22}$$

$$\langle c\rangle = \frac{\left[\int_0^{R_p(t)} c\,(4\pi r^2)\,dr\right]}{\frac{4}{3}\pi\left[R_p(t)\right]^3} \tag{3.1.23}$$

$$x = \left(\frac{c}{c_{max}}\right)\left[\frac{R_p(t)}{\lambda^{\frac{1}{3}}\,R_{p,o}}\right]^3 \tag{3.1.24}$$

3.1.3 Squeezing Effect

In the sodiation process of tin, a volume expansion of 420% was observed [59]. In such a situation, porosity changes in the electrode cannot be ignored. Garrick et al developed a model [90] to account for stresses built in the electrode due to volume changes. This model includes both - porosity changes and electrode dimension changes depending on the compressibility of the electrode casing.

Gomadam et al provided a governing equation for volume change based on the mass balance of the solid phase [91]. With the assumption of equal expansion in all directions, equation 3.1.25 is obtained.

$$\frac{\partial}{\partial t}(1-\varepsilon) + (1-\varepsilon)\frac{\partial \varphi}{\partial t} = -\frac{s\Delta\hat{V}}{nF}j \tag{3.1.25}$$

Here, ε represents the porosity of the electrode, φ represents the electrode volumetric strain, s represents the stoichiometric coefficient of product, $\hat{V}$ represents the molar volume of reaction product and j represents the local volumetric electrochemical reaction rate.

Garrick et al used the following assumptions in this formulation -

- The material expands equally in all directions.
- The reaction current is constant.
- No macroscopic gap is formed between the electrode and casing.
- Only small deformations exist implying that casing strain is proportional to stress.

Solving the material balance along with the aforementioned assumptions gives the following relations (equation 3.1.26 to 3.1.28) between porosity, stress and volume expansion.

$$\varphi = C_C\sigma \tag{3.1.26}$$

In equation 3.1.26, C_c represents the Casing compressibility and σ represents the hydrostatic stress.

$$\bar{\sigma} = \left[\frac{\Delta\hat{V}}{\hat{V}_{avg}}\right]\tau + \frac{1}{\gamma} LambertW\left(\gamma e^{-\left[\frac{\Delta\hat{V}}{\hat{V}_{avg}}\right]}\right) - 1$$

(3.1.27)

$\bar{\sigma}$ represents the dimensionless hydrostatic stress, τ represents the state of charge, γ represents the relative compressibility (ratio of electrode compressibility to casing compressibility) and $\hat{V}_{avg}$ represents the average molar electrode volume. *LambertW(x)* stands for the Lambert W function or the omega function [92].

$$\begin{aligned}\varepsilon(\bar{\sigma}) = e^{-\bar{\sigma}}\big(e^{\bar{\sigma}} & \\ + (1-\varepsilon^0)\left[\gamma e^{(\gamma-1)}\left(Ei(\gamma-1) - \bar{\sigma}(1-\gamma) - Ei(\gamma-1)\right)\right. & \\ \left. + e^{-1}\left(Ei(\gamma-1) - Ei(-1)\right) - 1\right] + \varepsilon^0\big) & \end{aligned}$$

(3.1.28)

ε_0 represents the initial porosity and *Ei(x)* is the first order exponential integral function [93].

The calculated value of porosity and volumetric strain can then be used to calculate the new electrode thickness, electrode area and electrode ionic resistance using equations 3.1.29-31. These values are then given by -

$$\frac{R}{R^o} = \frac{\frac{L}{L^o}}{\left(\frac{A}{A^o}\right)\left(\frac{\varepsilon}{\varepsilon^o}\right)^{1.5}} \quad (3.1.29)$$

$$\frac{L}{L^o} = \left(\frac{V}{V^o}\right)^{\frac{1}{3}} = (1+\varphi)^{\frac{1}{3}} \quad (3.1.30)$$

$$\frac{A}{A^o} = \left(\frac{V}{V^o}\right)^{\frac{2}{3}} = (1+\varphi)^{\frac{2}{3}} \quad (3.1.31)$$

3.2 Morphology changes

Until now, tin particles were assumed to be spherical in nature. However, some of the intermediate stages of Na-Sn were seen to have complex morphologies such as flake like particles.

In this work, the performance of nanosphere particles has been compared to that of nanorods. While most of the governing equations remain the same, the solid phase diffusion will change.

Nano-rods

While analyzing the system for nanorods, it will be assumed that the flow of sodium through the circular portions of the rods is insignificant compared to the curved surface. It will also be assumed that only the radius of the rod will increase when volume expansion takes place.

Equation 3.2.1 represent solid phase diffusion equation, given by Fick's law and equation 3.2.2 is the equation for the area of a nanorod.

$$\frac{\partial c_j}{\partial t} = \frac{D_j}{r}\frac{\partial}{\partial r}\left(r\frac{\partial c_j}{\partial r}\right) \tag{3.2.1}$$

$$S_j = 2\,\pi\,R_p L_o \tag{3.2.2}$$

The problem can then be solved using the formulation in section 3.1.2. However, for this geometry, the normalized current and concentration will change and is re-formulated in equation 3.2.3 and 3.2.4.

$$i' = i\left[\frac{R_{p,0}}{R_p(t)}\right]^2 \tag{3.2.3}$$

$$c'_{surf} = c_{surf}\left[\frac{R_p(t)}{R_{p,0}}\right]^2 \tag{3.2.4}$$

The maximum concentration of sodium is an intrinsic property of the material. Hence it will not change. However, the expression for state of charge will get modified and is given in equation 3.2.5.

$$x = \left(\frac{c}{c_{max}}\right)\left[\frac{R_p(t)}{\lambda^{\frac{1}{3}} R_{p,o}}\right]^3 \qquad (3.2.5)$$

The performance of these nanorods will be compared to the nanospheres in Chapter 4.

3.3 Finite Volume Formulation

The finite volume method is a technique to solve partial differential equations (PDE) by discretizing the domain into non-overlapping volumes over which quantities of interest are conserved.

The center of this volume is called a node. It is assumed that each of the conserved quantities has a single value over the volume, at the node. Using a single value per volume instead of a distribution significantly reduces computational time.

The process involving the following steps -

1. Grid generation
2. Discretization of the equation
3. Solving the set of equations

Grid Generation

Figure 3.3 represents the typical grid nomenclature used to solve a 1-D problem using this technique. The representative volume is marked by the dashed lines (-). Point *'P'* is a node at the center of the volume. Point *'W'* and point *'E'* are the nodes to the west and east of the current node. *'w'* and *'e'* represent the east and west walls of the volume in question. The length of the volume is given by Δx which is the sum of the distance between the center and the east wall (δx_{Pe}) and the distance between the center and west wall (δx_{wP}). The distance between the node and the east node is given by δx_{PE} and the distance between the node and west node is given by δx_{WP}.

In case there is a non-uniform grid, i.e. a case where $\delta x_{PE} \neq \delta x_{PW}$, the boundaries of the volume are chosen such that $\delta x_{Pe} = \frac{1}{2}\delta x_{PE}$ and$\delta x_{wP} = \frac{1}{2}\delta x_{WP}$.

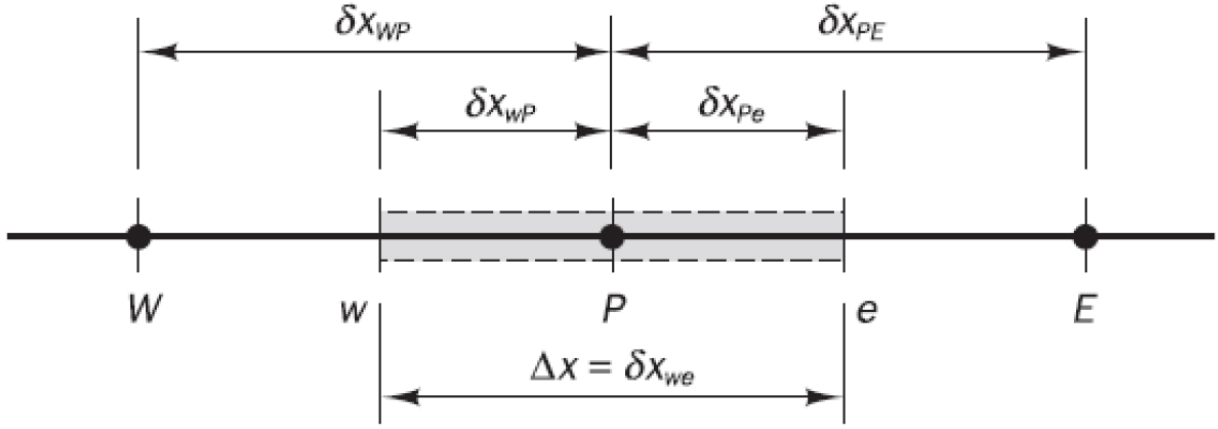

Figure 3.1. Representation of a Finite Volume Method grid.

The process mentioned above can similarly be extended for a 2D and 3D grid. For instance, while conserving the quantity over a 2D grid, a north and south node also need to be considered.

The diffusion equation in the single particle model is 1 dimensional in space. Hence a similar grid is generated along the radial direction. The particle radius Rpwas divided into 50 grid points for solving this problem. In addition, since the problem is a transient problem, the grid also evolves with time.

Discretizing the governing equation

Once the grid is generated, the equation needs to be discretized. In order to do this, the equation is integrated over the representative volume, known as the control volume.

Each volume provides one equation which relates the conserved quantities between different nodes in the domain. For ‘n’ control volumes, a set of ‘n’ equations are obtained.

The transient diffusion equation is integrated over time and volume as given in equation 3.3.1.

$$\int_{\Delta V}\int_{\Delta t}\frac{\partial c}{\partial t}=\int_{\Delta V}\int_{\Delta t}\frac{D}{r^2}\frac{\partial}{\partial r}\left(r^2\frac{\partial c}{\partial r}\right) \tag{3.3.1}$$

$$LHS=\frac{4}{3}\pi(r_e^3-r_w^3)\left(c_P^j-c_P^{j-1}\right)=\Delta V\left(c_P^j-c_P^{j-1}\right) \tag{3.3.2}$$

$$\begin{aligned}RHS&=\Delta t\int_{r_w}^{r_e}\frac{D}{r^2}\frac{\partial}{\partial r}\left(r^2\frac{\partial c}{\partial r}\right)4\pi r^2\,dr\\&=4\pi D\Delta t\left(\left[r^2\frac{\partial c}{\partial r}\right]_{r=r_e}-\left[r^2\frac{\partial c}{\partial r}\right]_{r=r_w}\right)\\&=4\pi D\Delta t\left(r_e^2\left(\frac{c_E^j-c_P^j}{\Delta r}\right)-r_w^2\left(\frac{c_P^j-c_W^j}{\Delta r}\right)\right)\end{aligned} \tag{3.3.3}$$

For all internal nodes, the discretized equation can be rearranged as shown below. This gives a set of equations for all internal nodes.

$$\left(1+\frac{4\pi D\Delta t r_e^2}{\Delta V\Delta r}+\frac{4\pi D\Delta t r_w^2}{\Delta V\Delta r}\right)c_P^j-\frac{4\pi D\Delta t r_e^2}{\Delta V\Delta r}c_E^j-\frac{4\pi D\Delta t r_w^2}{\Delta V\Delta r}c_W^j=c_P^{j-1}$$

$$(1+a_E+a_W)c_P^j-a_Ec_E^j-a_Wc_W^j=c_P^{j-1} \tag{3.3.4}$$

The boundary conditions will affect the discretization of the nodes close to the boundary.

Node 1: Closest to r = 0

For the node closest to r = 0, the west face of the volume coincides with the center of the particle. The boundary condition at r = 0 is given by equation 3.3.5. This condition is substituted into the discretized equation.

$$\left(D_j\frac{\partial c_j}{\partial r}\right)_{r=0}=0 \tag{3.3.5}$$

$$\begin{aligned}RHS&=\Delta t\int_{r_w=0}^{r_e}\frac{D}{r^2}\frac{\partial}{\partial r}\left(r^2\frac{\partial c}{\partial r}\right)4\pi r^2\,dr\\&=4\pi D\Delta t\left(\left[r^2\frac{\partial c}{\partial r}\right]_{r=r_e}-\left[r^2\frac{\partial c}{\partial r}\right]_{r=0}\right)\end{aligned}$$

$$= 4\pi D\Delta t r_e^2 \left(\frac{c_E^j - c_P^j}{\Delta r}\right) \tag{3.3.6}$$

The discretized equation can be rearranged as shown below in equation 3.3.7.

$$\left(1 + \frac{4\pi D\Delta t r_e^2}{\Delta V \Delta r}\right) c_P^j - \frac{4\pi D\Delta t r_e^2}{\Delta V \Delta r} c_E^j = c_P^{j-1}$$

$$(1 + a_2)c_1^j - a_2 c_2^j = c_1^{j-1} \tag{3.3.7}$$

Node 'N': Closest to r = R_p

For the node closest to r = R_p, the east face of the volume coincides with the surface of the particle. The boundary condition at r = R_p is given by equation 3.3.8. This condition is substituted into the discretized equation.

$$\left(D_j \frac{\partial c_j}{\partial r}\right)_{r=R_j} = -J_j \tag{3.3.8}$$

$$\begin{aligned} RHS &= \Delta t \int_{r_w}^{r_e = R_p} \frac{D}{r^2} \frac{\partial}{\partial r}\left(r^2 \frac{\partial c}{\partial r}\right) 4\pi r^2 \, dr \\ &= 4\pi\Delta t \left(-r_e^2 J - \left[D r^2 \frac{\partial c}{\partial r}\right]_{r = r_w}\right) \\ &= 4\pi\Delta t \left(-r_e^2 J - D r_w^2 \left(\frac{c_P^j - c_W^j}{\Delta r}\right)\right) \end{aligned} \tag{3.3.9}$$

The discretized equation can be rearranged as shown in equation 3.3.10 below.

$$\left(1 + \frac{4\pi D\Delta t r_w^2}{\Delta V \Delta r}\right) c_P^j - \frac{4\pi D\Delta t r_w^2}{\Delta V \Delta r} c_W^j = c_P^{j-1} - \frac{4\pi\Delta t r_e^2 J}{\Delta V}$$

$$(1 + a_{N-1})c_N^j - a_{N-1} c_{N-1}^j = c_N^{j-1} + b_N \tag{3.3.4}$$

After accounting for a boundary conditions, the following set of equations are obtained -

Node i = 1: $(1 + a_2)c_1^j - a_2c_2^j = c_1^{j-1}$ (3.3.7)

Node i = 2, 3…., N-1: $(1 + a_E + a_W)c_P^j - a_Ec_E^j - a_Wc_W^j = c_P^{j-1}$ (3.3.4)

Node i = N: $(1 + a_{N-1})c_N^j - a_{N-1}c_{N-1}^j = c_N^{j-1} + b_N$ (3.3.10)

Solving the set of equations

These equations can then be arranged into a matrix form AX = B and can be solved to obtain the concentration at each time step. In this work, the matrix was solved using the in MATLAB.

It should be noted that while discretizing the equation with respect to time, the values of concentration were chosen at two-time steps 'j' and 'j-1'. This is known as the implicit scheme. This scheme was used as it is stable for all values of the time step.

Alternatively, the equation could have been solved at time steps 'j' and 'j+1'. It would then be known as the explicit method. While this scheme is easier to implement and faster to solve, it is not unconditionally stable. The maximum time step that can be used is limited by the diffusivity and the r value. Hence this scheme was used in this simulation.

3.4 Material Properties of Tin Phosphide Particles

Table 3.1 has properties to be used in the Single Particle Model described in *M. Guo et al [72]*. The properties have been found for a system with a Na ion battery with an Sn based electrode. Some of the properties are based on the experimental data provided in *J. Qian et al [76]*.

Table 3.1. Properties used as inputs in the Single Particle Model for Sn_4P_3.

Electrochemical Property		**Expression / Value**	**Reference**
Diffusivity of Na [m^2/s]	D_{Na}	3.66 x 10^{-12} at 298 K $D_{Na} = D_0 exp\left(\frac{E_a}{k_b T}\right)$ D_0 = 0.9 x 10^{-7} [m^2/s] E_a = 0.26 [eV]	[95]
Total Electroactive Area [m^2]	S	$S = \frac{3\varepsilon A t}{R_p} = 0.0321$	Calculated
Exchange Current Density (Sn_4P_3/C)	i_0	$i_o = \frac{RT}{nFR_{ct}}$ R_{ct} = 30.6 [ohm]	[97]
Theoretical Capacity [mAh/g]	C_{th}	1132	[76]
Maximum Concentration of Na ions [mol/m^3]	C_{max}	24793	Calculated
Electrolyte Concentration [mol/m^3]	c_e	1000	[76]
Electrolyte Resistance [ohm]	R_{cell}	0	Assumption
Open Circuit Potential [V]*	OCP	OCP= -0.2907 logx-0.0853 x = State of Charge	[76]
Electrons involved		24	

Material Property		**Expression / Value**	**Reference**
Particle Size of Sn_4P_3 [nm]	R	100	[76]
Cell Area [m^2]	A	3.14 x 10^{-4}	[76]
Mass Loading [mg/cm^2]		2	[76]
Mass of Sn_4P_3 [g]		M = Loading * A= 0.0063	Calculated
Density of CMC [kg/m3]	ρ_{CMC}	350 - 600	[98]
Density of Super P [kg/m3]	ρ_P	160	[99]
Density of Carbon Black [kg/m^3]	ρ_C	1800 - 2100	[100]
Density of Sn_4P_3 [kg/m^3]	ρ_{AM}	5870	[96]

Table 3.1 continued

Volume fraction of active material	S	0.187 - 0.224 **(0.205)**	Calculated
Electrode Thickness [um]	t	$t = \frac{Loading}{\varepsilon_s \rho_{AM}}$	Calculated
Volume Expansion of Na_3P		490%	
Volume Expansion of $Na_{15}Sn_4$		520%	

Property		**Expression / Value**	**Reference**
Gas constant [J/mol-K]		8.314	
Faraday Constant [C/mol]		96485.332	

Property (Extra effects)		**Expression / Value**	**Reference**
Poisson Ratio	v	0.25	Assumption
Bulk Modulus (GPa)	B	20	[94]
Young's Modulus [GPa]	K	12.78	Calculated
Partial Molar Volume	**Ω**	1.468 x 10+-5	Calculated
Electrode Compressibility (GPa^{-1})	C_E	$C_E = 1 / B = 0.04$	Calculated
Casing Compressibility (GPa^{-1})	C_C	0.01	Assumption
Electrode Volume expansion coefficient		0.2	Assumption
Initial Porosity	0	0.5	Assumption

*OCP has been assumed to be equal to the discharge plot for a C rate of C/11.

3.5 Material Properties of Tin Particles

Table 3.2 has properties to be used in the Single Particle Model described in *M. Guo et al [72]*. The properties have been found for a system with a Na ion battery with an Sn based electrode.

Table 3.2. Properties used as inputs in the Single Particle Model for tin.

Electrochemical Property		**Expression / Value**	**Reference**
Diffusivity of Na [m^2/s]	D_{Na}	3.66 x 10^{-12} at 298 K $D_{Na} = D_0 exp\left(\frac{E_a}{k_b T}\right)$ D_0 = 0.9 x 10^{-7} [m^2/s] E_a = 0.26 [eV]	[95]
Exchange Current Density (Sn)	i_0	$i_o = \frac{RT}{nFR_{ct}}$ R_{ct} = 47.8 [ohm]	[40]
Theoretical Capacity [mAh/g]	C_{th}	847	Calculated
Electrolyte Concentration [mol/m^3]	c_e	1 M	From experiment
Electrolyte Resistance [ohm]	R_{cell}	0	Assumption
Open Circuit Potential [V]*	OCP		From experiment
Electrons involved		15	

Material Property		**Expression / Value**	**Reference**
Particle Size of Sn [um]	R	1	From experiment
Cell Area [m^2]	A	8.0384 x 10^{-4}	From experiment
Mass of Sn (mg)		2.94	From experiment
Density of Sn[kg/m^3]	ρ_{AM}	7300	[101]
Volume Expansion of $Na_{15}Sn_4$		520%	

Property		**Expression / Value**	**Reference**
Gas constant [J/mol-K]		8.314	
Faraday Constant [C/mol]		96485.332	

Table 3.2 continued

Property (Extra effects)		**Expression / Value**	**Reference**
Poisson Ratio of Sn	v	0.33	[101
Bulk Modulus of Sn (GPa)	B	42	[101]
Young's Modulus [GPa]	K	43	[101]
Casing Compressibility (GPa^{-1})	C_C	0.01	From expt
Electrode Volume expansion coefficient		0.2	Assumption
Initial Porosity	0	0.32	From expt

Calculated Quantities		**Expression**	**Reference**
Maximum Concentration of Na ions [mol/m^3]	C_{max}	49435	Calculated
Particle Electroactive Area [m^2]	S	$S = 4\pi R_p^2 = 1.256 * 10^{-11}$	Calculated
Electrode Thickness [um] (estimate is 10-15 um)	t	$t = \frac{Loading}{\varepsilon_s \rho_{AM}}$	Calculated
Electrode Compressibility (GPa^{-1})	C_E	C_E = 1 / B = 0.0238	Calculated

3.6 Fracture Model

Barai et al developed a model that was able to capture the two-phase diffusion process in the lithiation of alloying electrodes such as tin and silicon [102]. This model was also able to capture the stresses due to the large volume expansion in these electrodes. This model was later modified to capture the reduced mechanical degradation due to creep relaxation in lithiated tin electrodes [88]. In this thesis, the model has been applied to predict cracks in sodiated tin.

In high capacity materials, two phase diffusion is seen to take place [103]. Since Fick's law of diffusion is only applicable to single phase processes, the Cahn Hilliard equation is used [104] as given in equation 3.6.1. The boundary conditions are the same as that of the single particle model and are given in equation 3.6.2 and 3.6.3.

$$\frac{\partial \hat{c}_s}{\partial t} = \nabla M_{Na}(\hat{c}_s)\, \nabla\left\{c_{s,max} RT\left[\omega(1-2\hat{c}_s) + ln\frac{\hat{c}_s}{1-\hat{c}_s}\right] - \kappa\nabla^2\hat{c}_s\right\} \tag{3.6.1}$$

$$\left(\frac{\partial \hat{c}_s}{\partial r}\right)_{r=0} = 0 \tag{3.6.2}$$

$$M_{Na}(\hat{c}_s)\, \nabla\left\{c_{s,max} RT\left[\omega(1-2\hat{c}_s) + ln\frac{\hat{c}_s}{1-\hat{c}_s}\right] - \kappa\nabla^2\hat{c}_s\right\}_{r=1} = \frac{I}{SF} \tag{3.6.3}$$

$\hat{c}_s$ represents the state of charge of electrode, M_{Na} represents the concentration dependent mobility of sodium in the solid phase, R is the universal gas constant, T is the temperature, ω is a non-dimensional parameter signifying the enthalpy of mixing, κ accounts for the free energy at the phase boundary due to the concentration. This fourth order equation is solved by converting the fourth order equation to two second order equations. In addition, the particles are assumed to be spherical and hence only radial diffusion is considered. A detailed technique to solve this equation is given in the article by Barai and Mukherjee [102].

The evolution of fracture is solved using the lattice spring model. This model was previously used to solve fracture evolution in graphite. Since the volume expansion in graphite is small, the model used a linear stress strain relationship. When Barai et al extended this model for lithiated tin, a non-linear stress strain relation had to be used to account for the large volume expansion [88]. The governing differential equation to predict fracture is given in equation 3.6.4.

$$\int_V {}^{t+\Delta t}_{t}S_{ij}\,\delta\, {}^{t+\Delta t}_{t}\varepsilon_{ij}\, dV - \int_A {}^{t+\Delta t}_{t}F_i\,\delta\, {}^{t+\Delta t}_{t}u_i\, dA = {}^{t+\Delta t}R \tag{3.6.4}$$

V and A represent the volume and area at the previous equilibrium configuration. ${}^{t+\Delta t}_{t}S_{ij}$ is the 2nd Piola - Kirchoff tensor, ${}^{t+\Delta t}_{t}\varepsilon_{ij}$ is the Green-Lagrange strain tensor, ${}^{t+\Delta t}_{t}F_i$ is the externally applied force, ${}^{t+\Delta t}_{t}u_i$ is the displacement and ${}^{t+\Delta t}R$ is the residual. The first term in equation 3.6.4 represents the internal energy and the second term represents the energy due to the external forces.

There are two sources of strain in the system - volume expansion and creep deformation. The strain due to volume expansion is given in equation 3.6.5 and the strain due to creep deformation is given in equation 3.6.6.

$$\Delta\varepsilon^{chem} = \Delta\hat{c}_s \Omega c_{s,max} \tag{3.6.5}$$

$$\Delta\varepsilon^{chem} = A\left(\frac{max(0.0\,, F_{axial})}{G}\right)^n \Delta t \tag{3.6.6}$$

$\hat{c}_s$ is change in concentration, Ω is the volume expansion coefficient, *A* is a constant value representing the creep coefficient, *G* is the shear modulus of the spring elements and *n* is the stress exponent.

The spring stretches due to both the chemical and creep strain. The total length after deformation is given in equation 3.6.7. In the equation, $l_{elastic}$ represents the length of the string only due to elastic deformation.

$$l_{total} = l_{elastic}(1 + \Delta\varepsilon^{chem})(1 + \Delta\varepsilon^{creep}) \tag{3.6.7}$$

The strain energy within a spring element is given in equation 3.6.8. The element is considered broken if the strain energy exceeds the threshold fracture value. The fracture threshold value is distributed according to a uniform distribution. In the equation, f represents the incremental internal force and u represents an incremental displacement.

$$\psi_e^{n+1} = \psi_e^n + \frac{1}{2}\Delta\bar{f}\,.\,\Delta\bar{u} \tag{3.6.8}$$

Equation 3.6.1, representing diffusion, is solved using the Finite Difference Method (FDM). The volume expansion is fraction is solved by combining equations 3.6.4 - 3.6.8. It is a one - way coupled system where the transport affects the mechanics. The results obtained from this technique are presented in the next chapter.

4. RESULTS

This chapter is divided into 5 sections. The first section validates the performance model built in this thesis by comparing the simulated performance to experimental results from literature. In the second section, some of the cell's parameters are changed to observe their effect on the performance of the cell's capacity. In the third section, the change in performance due to the 2 additional effects - squeezing and volume expansion is investigated. In the fourth section, two additional particle morphologies are investigated and their effect on the performance is explored. In the last section, mechanical degradation of tin particles is simulated.

4.1 Validation of Model

The first step to understand the validity of the model is to compare it with a set of experimental results for the material. This model was validated for two anode materials - tin and tin phosphide. For tin phosphide, the simulation results were compared to the results published by Qian et al [76]. The experimental results for tin particles were provided by members from Dr Mukherjee's research group.

As seen in Chapter 3, all the material properties for the electrodes are not available in literature. For some of the quantities, there is a large variation in the properties in different articles. Hence there is a need to estimate some of the missing parameters before the model is simulated. For the sodium ion performance model, the following parameters need to be estimated -

1. Diffusivity of sodium ions
2. Reaction rate
3. Particle size
4. Cell electrolyte resistance

These parameters are varied until a good match is obtained between the simulation and experimental results.

4.1.1 Tin Phosphide

Qian et al synthesized an Sn_4P_3 nano-composite and observed a very high reversible capacity of 850 mAh/g [76]. They also observed the rate performance of the material for charge rates between 100 mA/g to 1000 mA/g. These rate plots were used to predict the parameters mentioned above.

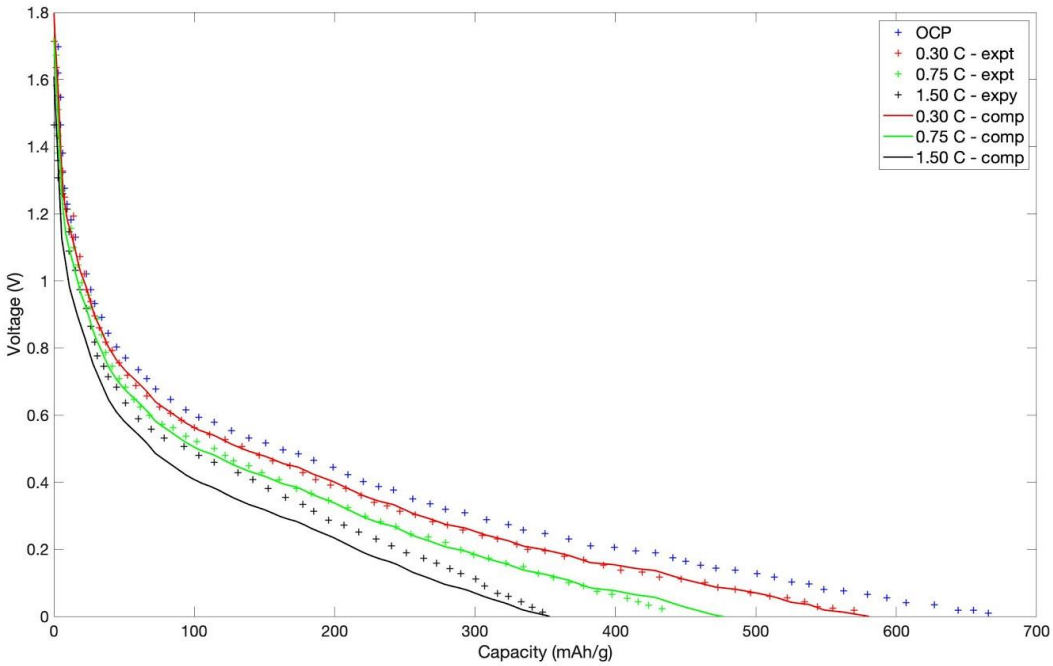

Figure 4.1. Comparison of simulation and experimental results for Sn_4P_3

One of the most important quantities for calculated cell voltage is the Open Circuit Potential (OCP) value. The OCP is typically found from GITT experiments. Unfortunately, the OCP value for tin-phosphide was not available in literature.

By definition, the OCP is the cell potential when there is zero current passing through the cell. Since the OCP value is not available, it needs to be estimated. The simplest way to estimate this value is to find a cell charging plot with a very low charge rate.

In the results published by Qian et al [76], a voltage vs capacity plot is available for a charge rate of 100 mA/g which corresponds to a very low charge rate of 0.1 C. Hence this plot will be used as

the OCP plot for the system. These values are used to predict the performance of the cell at higher charge rates.

The simulation was run at three different charge rates - 0.3 C, 0.75 C and 1.5 C. After running multiple iterations, the parameters which provided the best match between experimental and simulation results are listed in Table 4.1.

Table 4.1. Parameter values for Sn_4P_3 used in this study.

Parameter	**Symbol**	**Value**
Diffusivity of Na in Sn_4P_3 [m^2/s]	D_{Na}	7×10^{-17}
Reaction Rate [$(m/s)(mol/m^3)^{0.5}$]	k	16×10^{-13}
Particle Radius [nm]	R_P	95
Cell resistance [ohm]	R_{cell}	450

As seen in figure 4.1, a good match is obtained between experimental and simulation results for charge rates of 0.3 C and 0.75 C. For 1.5 C, it is seen that the simulation underpredicts the voltage values. This can be attributed to the fact that the electrolyte limits transport at high charge rates in the cell. However, the single particle model cannot capture this effect as the model neglects the effect of electrolyte while predicting the performance of the cell.

4.1.2 Tin

Experiments for tin were performed in the Energy and Transport Sciences Laboratory at Purdue University. The cell was charged and discharged at charge rates of C/10, C/20 and C/50.

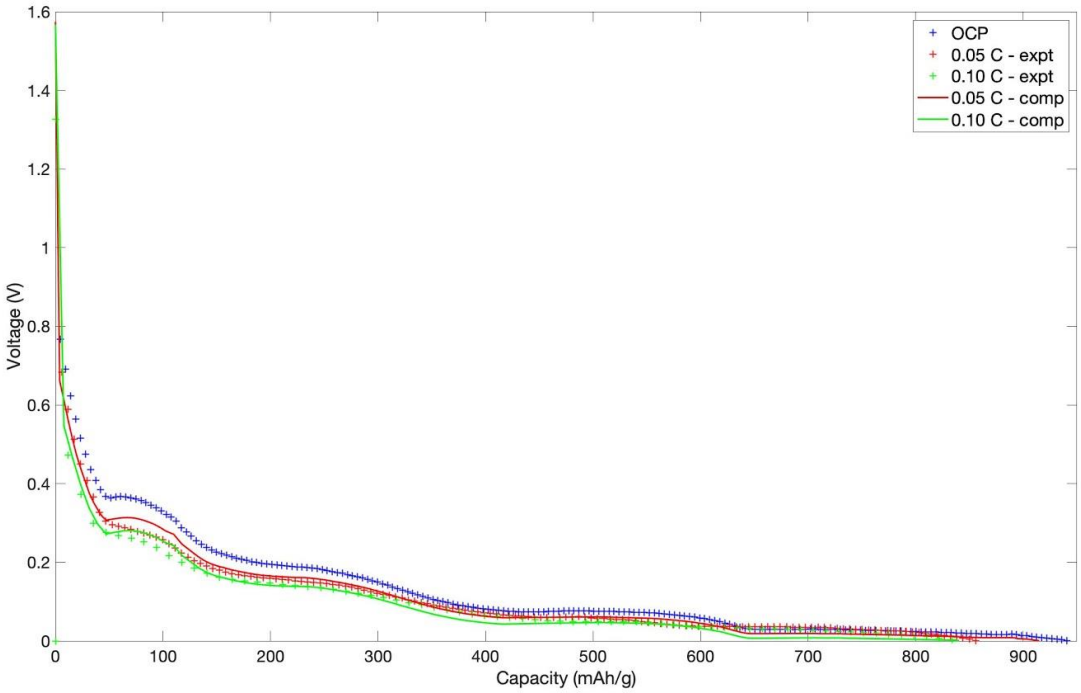

Figure 4.2. Comparison of simulation and experimental results for Sn.

Similar to tin phosphide, the OCP value for sodium intercalation in tin is not available. Hence, the voltage vs capacity plot for C/50 is treated as the OCP.

As seen in figure 4.2, the model predicts the voltage vs capacity plots reasonably well for charge rates of C/10 and C/20. The parameters used to obtain the plots are listed in table 4.2.

Table 4.2. Parameter values for Sn used in this study.

Parameter	**Symbol**	**Value**
Diffusivity of Na in Sn [m^2/s]	D_{Na}	7×10^{-13}
Reaction Rate [$(m/s)(mol/m^3)^{0.5}$]	k	3×10^{-13}
Particle Radius [nm]	R_P	1000
Cell resistance [ohm]	R_{cell}	80

4.2 Effect of changing simulation parameters

In this section, parameters such as the charge rate, diffusivity, particle size, reaction rate and the electrolyte resistance has been changed to observe the effect on the performance of the electrode.

4.2.1 Particle Size

The particle radius directly affects the available active area for diffusion. An electrode is made of a large number of spherical particles. When the radius of the particle increases, the surface area of each individual particle increases. However, the volume also increases implying a lesser number of particles available in the same active material mass.

Taking a closer look, the particle surface area is proportional to the square of the particle radius and the number of particles is inversely proportional to the cube of the radius. Hence the total surface area of the electrode is inversely proportional to the radius of the particle. A smaller surface area implies a larger current density which leads to a higher overpotential and hence a drop in the capacity of the cell.

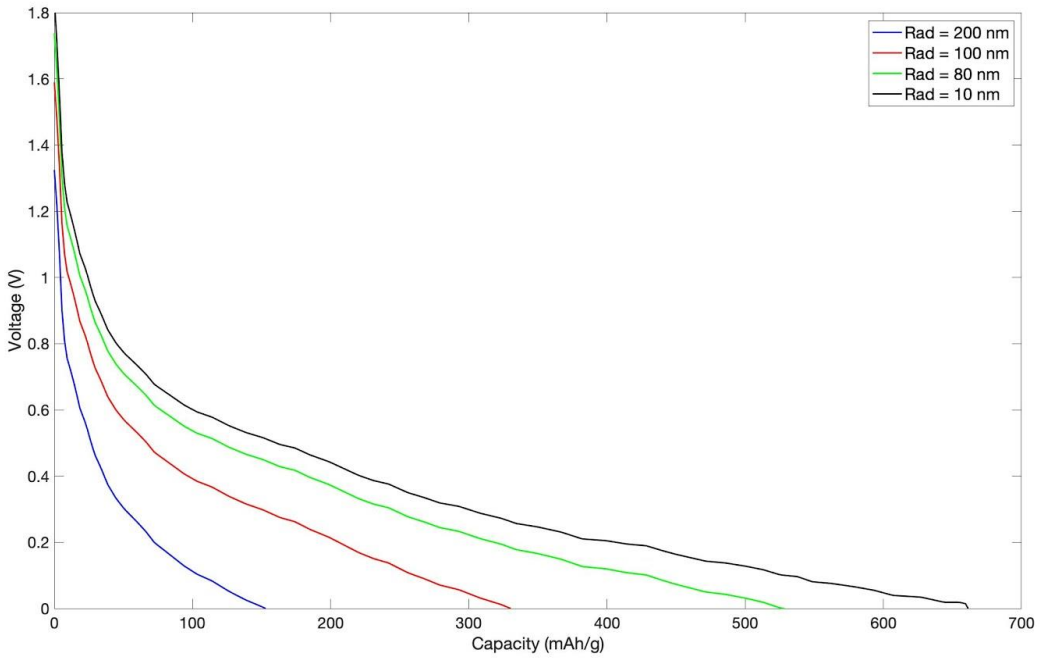

Figure 4.3. Effect of changing particle size on the electrode performance.

In Figure 4.3, the radius of the Sn4P3 particle was varied between 10 nm and 200nm. As theorized, the capacity significantly reduces as the radius of the particle is increased.

4.2.2 C-rate

The C-rate or charge rate is a measure of how fast a cell charges or discharges. A C-rate of C/2 implies that the entire cell discharges within 2 hours of operation. The cell is charged faster by using a larger current. Hence, a larger C-rate implies a larger current is charging/discharging the cell.

For the same particle surface area, a larger current implies a larger current density on the particle surface. Once again, as the current density increases, the overpotential increases and hence the capacity of the electrode decreases. In figure 4.4, it is seen that the electrode capacity decreases as the C-rate of the cell increases.

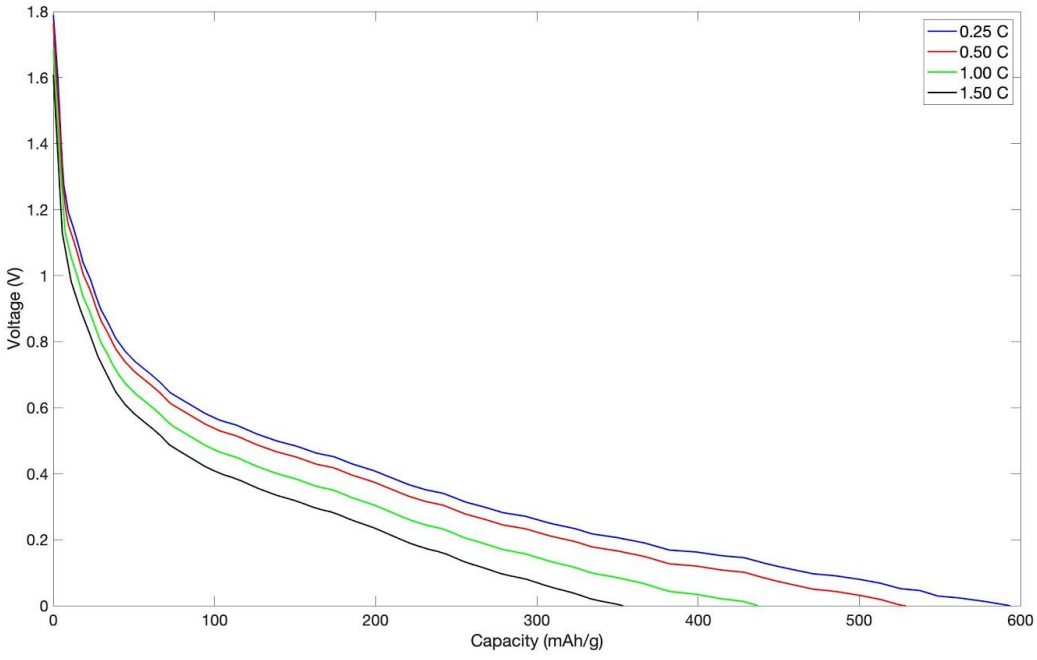

Figure 4.4. Effect of changing C-rate on the electrode performance.

4.2.3 Reaction rate

The reaction rate, in the context of an electrochemical cell, is the speed at which active material ions complete their intercalation process. A faster reaction rate implies that the charging/discharging process occurs easily in the cell.

When the reaction rate of the cell increases, the resistance of the cell to charge transfer decreases. This increases the exchange current density of the cell. As the exchange current density increases, the overpotential of the cell decreases improving the capacity of the cell.

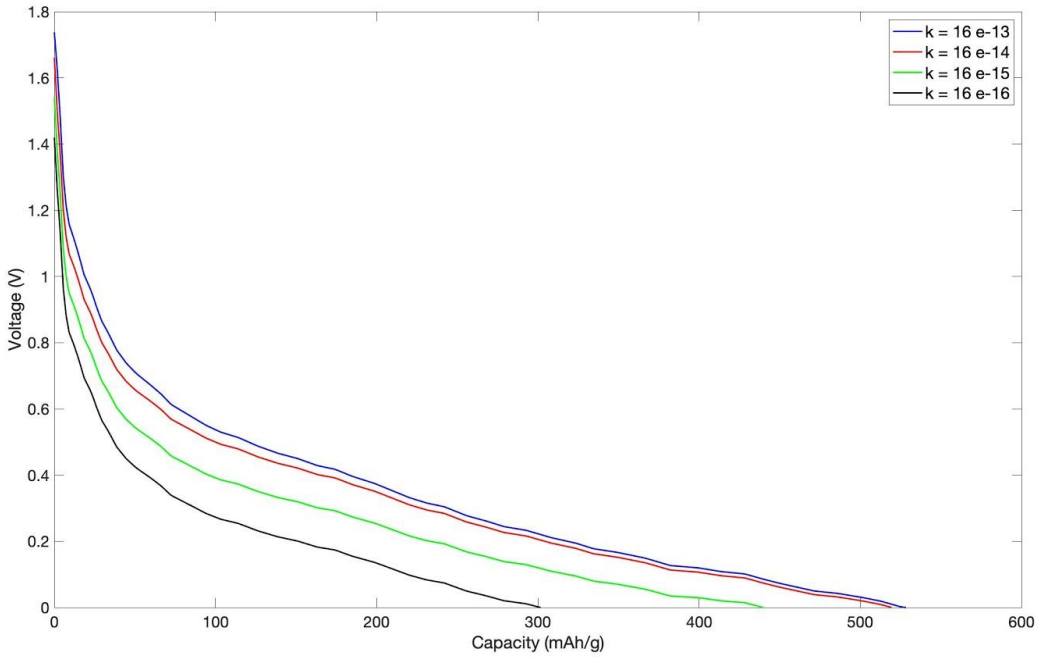

Figure 4.5. Effect of changing reaction rate on the electrode performance.

This effect is seen in Figure 4.5. The capacity of the electrode increases as the reaction rate increases. However, it is seen to remain constant for rate of the order of 10^{-13}. This is because there is almost zero resistance to charge transfer at this reaction rate.

4.2.4 Cell resistance

The single particle model neglects the local concentration distribution within the electrolyte. It assumes that the electrolyte does not limit transport in the cell reaction. Hence, the resistance of the electrolyte is treated as a single lumped quantity called the cell resistance.

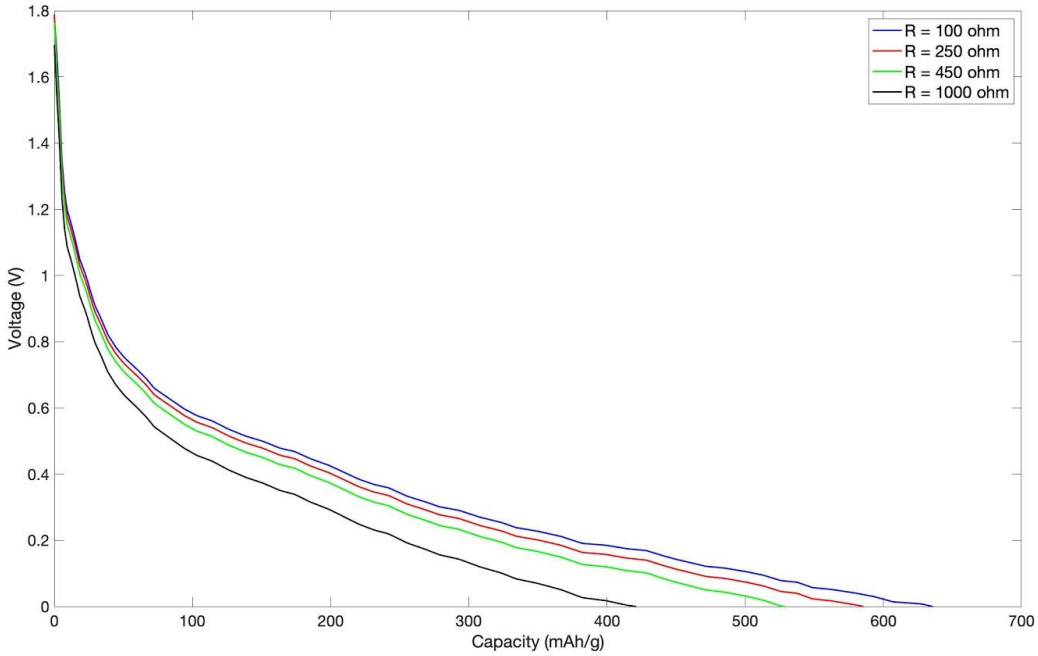

Figure 4.6. Effect of changing electrolyte resistance on cell performance.

This lumped cell resistance term is then used to calculate the electrolyte voltage which is subtracted from the cell voltage. Figure 4.6 represents the change in voltage vs capacity plot when the resistance is increased from 100 ohm to 1000 ohm. Since these plots have at the same C-rate, the difference in voltages between any two of these plots is a constant value.

4.2.5 Diffusivity of sodium

The diffusivity is a measure of how fast one material spreads into another. It is defined for a pair for species. For instance, the diffusivity of sodium ions is defined for the diffusion process into tin or tin phosphide. A higher diffusivity indicates that the species faces no resistance to moving or intercalating into the other species.

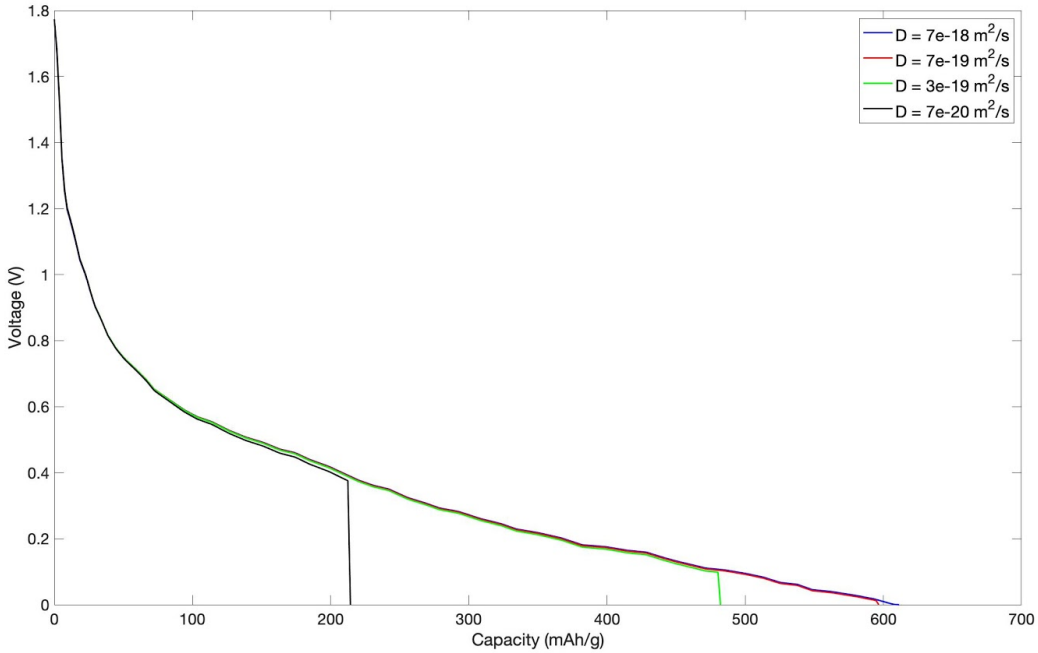

Figure 4.7. Effect of changing diffusivity on cell performance.

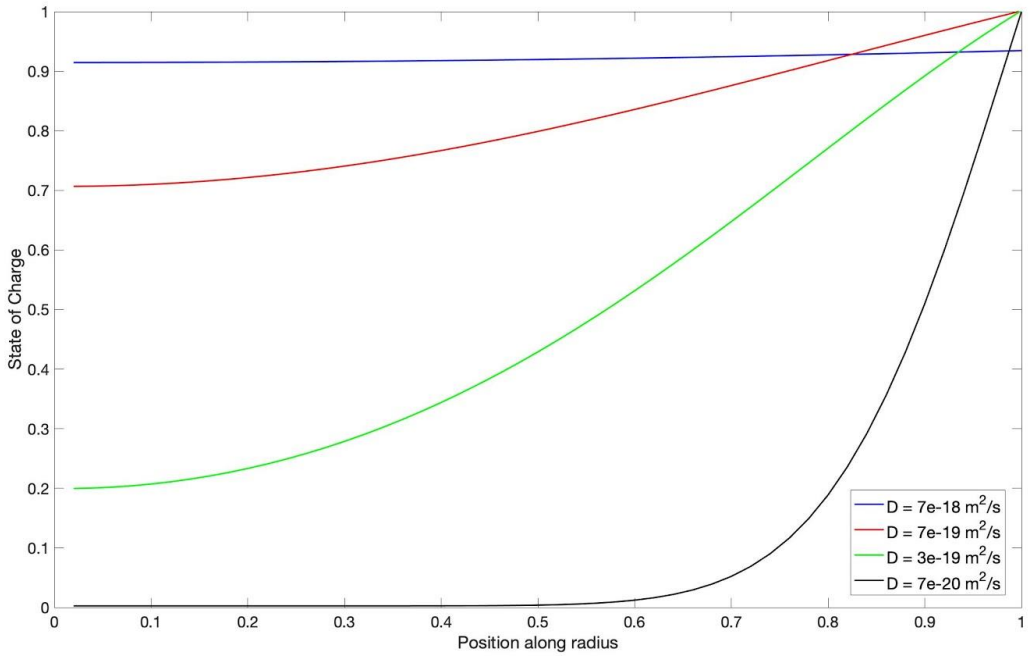

Figure 4.8. State of charge along particle radius for different diffusivity values.

When the diffusivity of sodium decreases, it becomes difficult for sodium ions to intercalate towards the center of the tin particles. Hence, charge accumulates at the surface and the surface concentration increases rapidly to reach the maximum value. The maximum concentration value is an intrinsic material property and hence is a constant. Once this value is reached, the simulation stops as the particle cannot incorporate any more sodium.

In Figure 4.7, it can be seen that for diffusivity values of 3×10^{-19} m^2/s and 7×10^{-20} m^2/s, the particle discharge abruptly stops at 480 mAh/g and 230 mAh/g respectively. This is the point where the maximum concentration has been reached at the surface.

Figure 4.8 represents the state of charge along the particle radius. At a high diffusivity value of 7×10^{-18} m^2/s, the sodium ions quickly diffuse into the particle. Hence the state of charge along the radius is the same. As the diffusivity is decreased, a concentration gradient builds up in the particle. For a diffusivity value of 7×10^{-20} m^2/s, it is seen that the state of charge at the center of the electrode is almost zero. This explains why the particle cannot accept more sodium ions.

4.3 Additional Effects in the Single Particle Model

As described in chapter 3, the single particle model was modified to account for the large volume expansion of tin. This section investigates the impact of each of the squeezing effect on the performance of the battery.

As discussed in chapter 2, the sodiation of tin creates a 420% expansion in the particle volume. A tin electrode consists of a large number of such particles. As these particles expand, the porosity of the electrode reduces. This expansion also generates stresses which could expand the electrode casing.

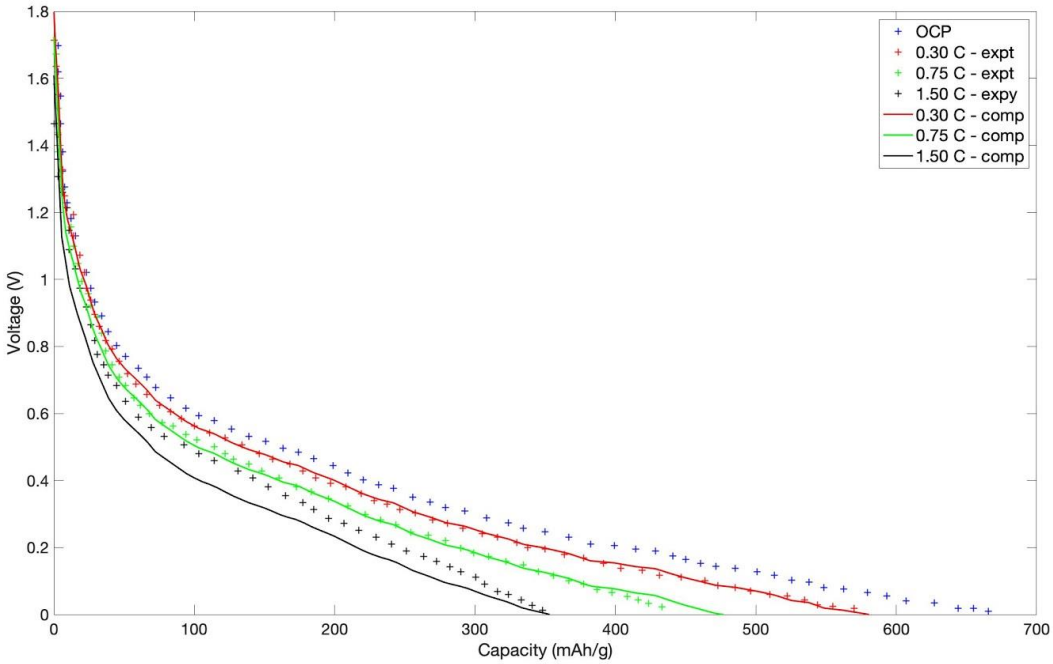

Figure 4.9. Simulation and experimental results for Sn_4P_3 with the squeezing effect.

If the casing is incompressible, the particles volumes would increase and the porosity would significantly decrease. If the casing had zero resistance, there would be no stress in the electrode and the volume of the electrode would expand. For most materials, the casing has a finite compressibility and hence both these effects take place - there is a decrease in porosity and an increase in electrode volume.

The extent to which these effects take place depends on the relative compressibility in the electrode. The relative compressibility is defined as the ratio of the electrode compressibility to the casing compressibility. In the formulation developed by Garrick et al [90], the casing strain and corrected porosity values affect the length of electrode, area of electrode and the electrolyte resistance.

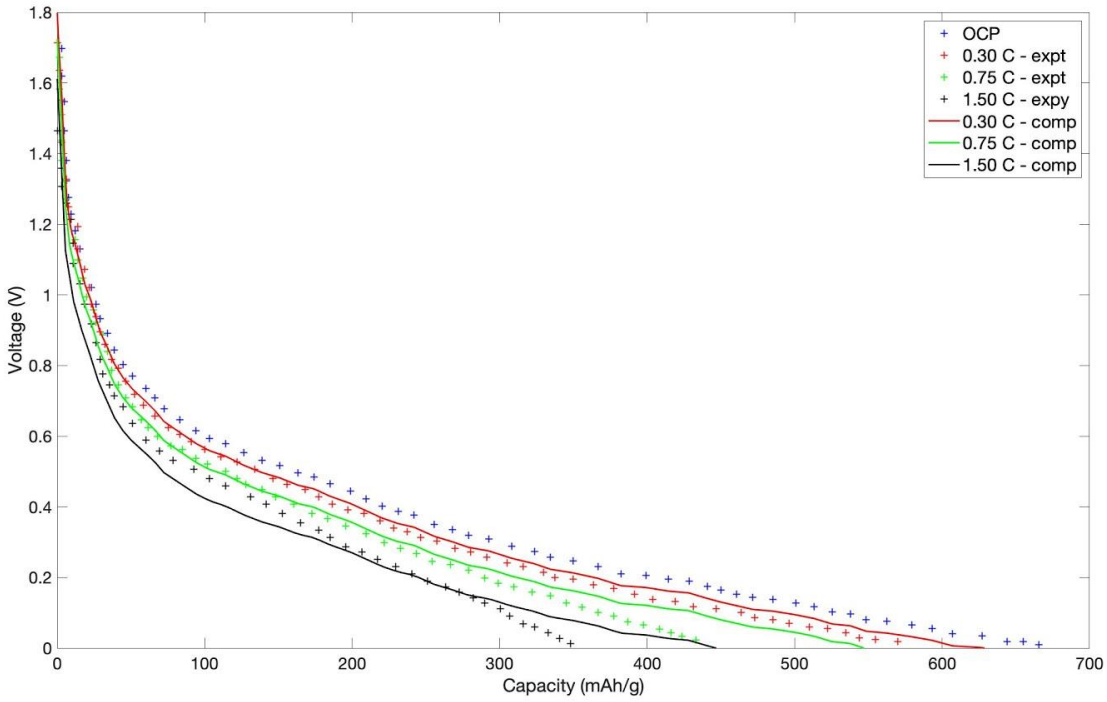

Figure 4.10. Simulation and experimental results for Sn_4P_3 without the squeezing effect.

Figure 4.9 is identical to Figure 4.1 and represents the first charging plots when the squeezing effect is included in the model. Figure 4.10 represents the first charging plots while neglecting the squeezing effect in the model. The effect has been neglecting by assuming that there is no casing strain and no porosity change. Similar to section 4.1, some of the parameters for the squeezing effect were not available in literature. These parameter values were found by getting a good match between simulation and experimental results. The parameters found by comparing the plots are listed in Table 4.3.

Table 4.3. Parameter values for the squeezing effect used for Sn_4P_3 simulations.

Parameter	**Symbol**	**Value**
Compressibility Ratio	γ	50
Electrode volume expansion coefficient	dV	0.2
Initial porosity	ε_0	0.32

Comparing Figure 4.7 and 4.8, it is seen that the addition of the squeezing effect decreases the capacity of the cell. This is because the porosity of the electrode decreases once this effect is included. This decrease in porosity increases the ionic resistance of the cell. Hence, the capacity of the cell reduces.

4.4 Morphology Changes

As discussed in chapter 3, the morphology of tin particles may not always be spherical in shape. Hence it is necessary to determine the change in performance in case the particle has a different shape.

In this section, the performance of a spherical particle is compared to that of a rod or cylindrical particle. The aspect ratio of the rod-shaped particle was varied while maintaining a constant particle volume. The capacities of the different particles are summarized in Table 4.4. The particle size used in this study was 95 nm and the diffusivity used was 3×10^{-19} m^2/s.

Table 4.4. Cell capacity for different particle morphologies and charge rates.

	C-rate = 0.3	**C-rate = 0.75**	**C-rate = 1.5**
Nanospheres	575 mAh/g	425 mAh/g	289 mAh/g
Nanorods (L/R = 1.33)	476 mAh/g	263 mAh/g	272 mAh/g
Nanorods (L/R = 4)	586 mAh/g	427 mAh/g	288 mAh/g
Nanorods (L/R = 10)	592 mAh/g	477 mAh/g	322 mAh/g

It is seen from Table 4.4 that particles of the same volume the capacity of the battery increases as the aspect ratio (L/R) of the nanorod increases. For the same particle volume, as the length of the rod increases, the radius decreases. As the radius decreases, the diffusivity limitations in the particle also decrease. This makes it is easier for sodium ions to intercalate into the rod. Hence, the capacity increases.

It is also seen as the aspect ratio increases beyond a threshold value, the nanorods perform better than the nanospheres. For the intercalation of sodium in tin phosphide, this threshold value was found to be close to 4.

4.5 Fracture Model

The fracture model developed by Barai et al for lithiation of tin has been extended and applied to the sodiation of tin. The simulation parameters used for crack prediction as listed in Table 4.5. It should be noted that all the parameters required for the simulation were not available in literature. In such cases, due to the similarity in the chemistries of lithium and sodium ion batteries, values for the lithiation process have been used instead.

Table 4.5. Material properties used in the fracture model.

Quantities		**Expression**	**Reference**
Diffusivity (m^2/s)	D_{Na}	3.66×10^{-12} at 298 K	[13]
Maximum sodium concentration in tin (mol/m^3)	c_{max}	44286	Calculated
Temperature (K)	T	300	Assumed
Non-dimensional enthalpy of mixing	ω	2.6	[26]
Gradient energy coefficient (J/m)	κ	2.0×10^{-9}	[26]
Young's modulus of amorphous Na_xSn (GPa)	E_a	25	[25]
Young's modulus of crystalline Sn (GPa)	E_c	50	[25]
Shear Modulus (GPa)	G	20	[25]

Table 4.5 continued

Fracture threshold energy of amorphous Na_xSn (J/m^2)	$\psi_{t,a}$	1.0	[42]
Fracture threshold energy of crystalline Sn (J/m^2)	$\psi_{t,c}$	4.0	[22]
Creep Exponent	n	1.1	[22]
Creep Coefficient	A	5.0×10^{-4}	[22]

In this work, particles of size 700 nm were lithiated at six different charge rates between 0.04 C and 2.00 C. Barai et al [88] have found a linear relationship between the strain rate in the particle and the charge rate. The two were seen to be related by a factor of 400. For instance, a charge rate of 1 C implies a strain rate of $2.5 \times 10^{-3}\ s^{-1}$.

Table 4.6 lists the charge rate vs fraction of broken bonds for the six charge rates used in the simulation. As expected, the number of broken bonds increases as the strain rate in the particle increases.

Strain Relaxation

Figure 4.10 (a) to (f) represent the fractured particle after the strain rate has been applied. When observed closely, it can be seen that figure (a) and (b), corresponding to charge rates of 0.04 C and 0.10 C, are larger than the rest of the figures. This expansion at low charge or strain rates can be explained by two effects - the creep relaxation and amount of sodium intercalated. At low C-rates, the amount of sodium intercalated is larger. Hence, the volume of the particle is larger.

Table 4.6. Effect of strain rate on the number of broken bonds.

C-Rate	**Strain Rate (s^{-1})**	**Number of Broken Bonds**	**Fraction of broken bonds**
0.04	1×10^{-4}	1300	0.1958
0.10	2.5×10^{-4}	1634	0.2461
0.25	6.25×10^{-4}	1938	0.2919
0.50	1.25×10^{-3}	2112	0.3181

Table 4.6 continued

1.00	2.5 x 10^{-3}	2177	0.3279
2.00	5 x 10^{-3}	2210	0.3329

At low strain rates, the particle expands in order to release the stresses built up within the particle. This expansion reduces the chance of crack propagation within the particle. It should be noted that this volume expansion is different from the expansion due to intercalation of sodium ions into the electrode. The intercalation volume expansion, in fact, increases the cracks in the particle.

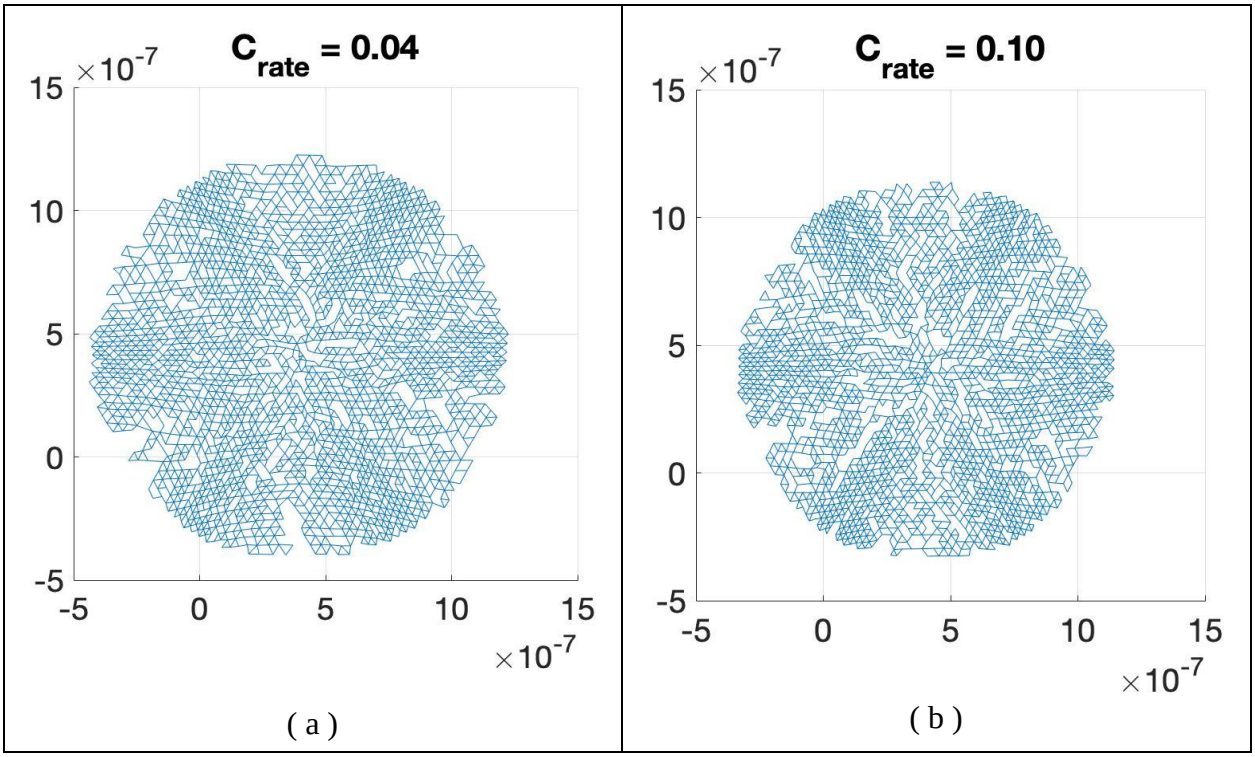

Figure 4.11. Microcrack formation on particles at different C-rates

Figure 4.11 continued

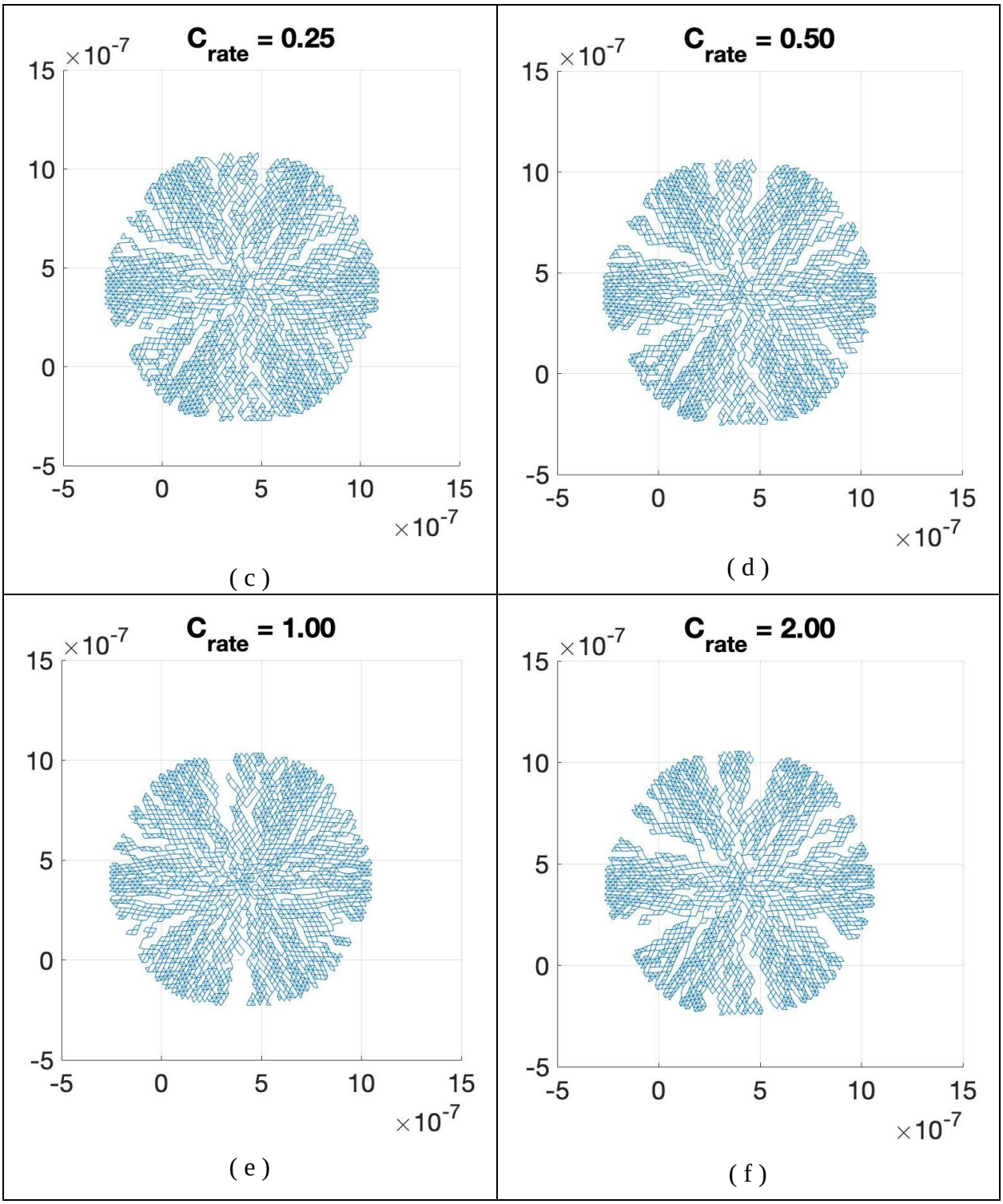

5. CONCLUSION AND FUTURE WORK

5.1 Conclusion

In this thesis, the process of sodiation in electrodes has been investigated. After an extensive literature review, tin was identified as an ideal electrode material for sodiation due to its high specific capacity, good cyclability and low electrode potential.

As part of this work, a battery performance model based on the single particle formulation has been developed. The model has been modified from the classical single particle model to capture large volume expansions in electrode materials. The model also accounts for the stresses induced in the electrode due to the porosity changes and compressibility of the casing.

This performance model was then validated using experimental results for tin (Sn) and tin phosphide (Sn_4P_3). This modified model successfully predicts the performance of the cell for C-rates of less than 1 C. It does not perform very well at high C-rates due to transport limitations of the single particle formulation. The performance of the modified model was also compared to a classical single particle model. It was determined that both the effects, the particle volume expansion and the electrode compressibility, play an equally important role in improving the prediction of the model.

Parametric studies were done to determine the effect of diffusivity, particle radius and reaction rate on the cell performance. The electrolyte resistance, treated as a lumped resistance term, was also varied to observe its effect.

Since micro or nano sized tin particles may not always be spherical in nature, the model was extended to predict performance for a cylindrical particle morphology. A parametric study was done to compare the performance of micro-spheres to micro-rods of different aspect ratios. For the tin phosphide system, it was observed that the nanorods have a better capacity than nanospheres beyond an aspect ratio of 4.

A lattice spring method-based fracture model was used to determine the relationship between strain rate and fracture in a tin particle. It was observed that the extent of fracture increases with an increase in strain rate in the particle. At low strain rates, it was also observed that creep deformation reduces the extent of fracture in electrode by increasing the volume of the particle. This phenomenon is known as strain relaxation and was observed at C-rates of less than 0.25 C.

5.2 Future Work

The performance and accuracy of a model heavily depend on experimental results which have been used to build the model. In this model, properties such as diffusivity and reaction rate were found by comparing simulation results to a set of experimental results. In the future, these properties could be found using experimental techniques and then included in the model.

In the single particle formulation, the open circuit potential (OCP) is one of the most important inputs that needs to be provided to the model. The OCP is found using Galvanostatic Intermittent Titration Technique (GITT) experiments. The Energy and Transport Sciences Laboratory at Purdue university is currently working on performing GITT experiments for micron size tin particles. Once the OCP is found, the voltage vs capacity plots predicted by the model will significantly improve.

A major limitation of the single particle model is the poor performance at high C-rates. In the future, the single particle formulation could be replaced with more robust models based on the porous electrode theory. This will extend the validity of the model.

Researchers have observed some additional effects taking place in electrodes due to large volume expansion. For instance, Zhang et al [108] have developed a model for diffusion induced stresses in the electrode. Additional governing equations can be added to include these effects in the model.

In the next few decades, battery research is going to transition to sodium-based technologies. An extensive study of sodium ion batteries is essential before they can be commercialized. Hence there is a lot of opportunity in the future to investigate the underlying physics and improve the quality of these models.

REFERENCES

[1] The Paris Agreement. (n.d.). Retrieved from https://unfccc.int/process-and-meetings/the-paris-agreement/the-paris-agreement

[2] Renewable Energy. (2017, November 1). Retrieved from https://www.c2es.org/content/renewable-energy/

[3] Sources of Greenhouse Gas Emissions. (2019, September 13). Retrieved from https://www.epa.gov/ghgemissions/sources-greenhouse-gas-emissions

[4] Volta A (1800) Philos Trans 2:430 (n.d.). Retrieved from http://rstl.royalsocietypublishing.org/site/misc/featuredarticles.xhtml.

[5] Scrosati, B. (2011, May 4). History of lithium batteries. Retrieved from https://link.springer.com/article/10.1007/s10008-011-1386-8.

[6] Leclanché G-L (1866) Compt Rend 83:54

[7] W.S. Harris, Ph.D. Thesis UCRL-8381, University of California, Berkeley.

[8] Whittingham MS (1978) Prog Solid State Chem 12:41

[9] Schalkwijk, W. V., & Scrosati, B. (2002). Advances in Lithium Ion Batteries Introduction. *Advances in Lithium-Ion Batteries*, 1–5. doi: 10.1007/0-306-47508-1_1

[10] M. Armand, in Materials for Advanced Batteries, D. W.Murphy, J. Broodhead, and B. C. H. Steele, Editors, p. 145, Plenum Press, New York (1980).

[11] Armand, M., Endres, F., Macfarlane, D. R., Ohno, H., & Scrosati, B. (2009). Ionic-liquid materials for the electrochemical challenges of the future. *Nature Materials*, *8*(8), 621–629. doi: 10.1038/nmat2448

[12] Yang, M., & Hou, J. (2012). Membranes in Lithium Ion Batteries. *Membranes*, *2*(3), 367–383. doi: 10.3390/membranes2030367

[13] Kim, S. , Seo, D. , Ma, X. , Ceder, G. and Kang, K. (2012), Electrode Materials for Rechargeable Sodium-Ion Batteries: Potential Alternatives to Current Lithium-Ion Batteries. Adv. Energy Mater., 2: 710-721.

[14] Chayambuka, K., Mulder, G., Danilov, D. L., Notten, P. H. L., *Adv. Energy Mater*. 2018, 8, 1800079.

[15] Slater, M. D., Kim, D. , Lee, E. and Johnson, C. S. (2013), Sodium-Ion Batteries. Adv. Funct. Mater., 23: 947-958.

[16] Naoaki Yabuuchi, Kei Kubota, Mouad Dahbi, and Shinichi Komaba Chemical Reviews 2014 *114* (23), 11636-11682

[17] Nagelberg, A. S., & Worrell, W. L. (1979). A thermodynamic study of sodium-intercalated TaS2 and TiS2. *Journal of Solid State Chemistry*, *29*(3), 345–354. doi: 10.1016/0022-4596(79)90191-9

[18] Delmas, C., Braconnier, J., Fouassier, C., & Hagenmuller, P. (1981). Electrochemical intercalation of sodium in NaxCoO2 bronzes. *Solid State Ionics*, *3-4*, 165–169. doi: 10.1016/0167-2738(81)90076-x

[19] Molenda, J., Delmas, C., & Hagenmuller, P. (1983). Electronic and electrochemical properties of NaxCoO2−y cathode. *Solid State Ionics*, *9-10*, 431–435. doi: 10.1016/0167-2738(83)90271-0

[20] Tarascon, J. (1986). Sodium intercalation into the layer oxides NaxMo2O4. *Solid State Ionics*, *22*(1), 85–96. doi: 10.1016/0167-2738(86)90062-7

[21] Jow, T. R. (1987). The Role of Conductive Polymers in Alkali-Metal Secondary Electrodes. *Journal of The Electrochemical Society*, *134*(7), 1730. doi: 10.1149/1.2100746

[22] Shacklette, L. W. (1988). Rechargeable Electrodes from Sodium Cobalt Bronzes. *Journal of The Electrochemical Society*, *135*(11), 2669. doi: 10.1149/1.2095407

[23] Ge, P. (1988). Electrochemical intercalation of sodium in graphite. *Solid State Ionics*, *28-30*, 1172–1175. doi: 10.1016/0167-2738(88)90351-7

[24] Stevens, D. A., & Dahn, J. R. (2000). High Capacity Anode Materials for Rechargeable Sodium-Ion Batteries. *Journal of The Electrochemical Society*, *147*(4), 1271. doi: 10.1149/1.1393348

[25] Range Assessment of Current Lithium Reserves. (n.d.). Retrieved from https://www.ffe.de/en/topics-and-methods/resources-and-climate-protection/666-range-assessment-of-current-lithium-reserves.

[26] Ellis, B., Makahnouk, W., Makimura, Y. *et al.* A multifunctional 3.5 V iron-based phosphate cathode for rechargeable batteries. *Nature Mater* **6,** 749–753 (2007) doi:10.1038/nmat2007

[27] Ma, X., Chen, H., & Ceder, G. (2011). Electrochemical Properties of Monoclinic NaMnO2. *Journal of The Electrochemical Society*, *158*(12). doi: 10.1149/2.035112jes

[28] Armstrong, A., Bruce, P. Synthesis of layered $LiMnO_2$ as an electrode for rechargeable lithium batteries. *Nature* **381,** 499–500 (1996) doi:10.1038/381499a0

[29] Komaba, S., Takei, C., Nakayama, T., Ogata, A., & Yabuuchi, N. (2010). Electrochemical intercalation activity of layered NaCrO2 vs. LiCrO2. *Electrochemistry Communications*, *12*(3), 355–358. doi: 10.1016/j.elecom.2009.12.033

[30] Didier, C., Guignard, M., Denage, C., Szajwaj, O., Ito, S., Saadoune, I., … Delmas, C. (2011). Electrochemical Na-Deintercalation from NaVO2. *Electrochemical and Solid-State Letters*, *14*(5). doi: 10.1149/1.3555102

[31] J. Li , J. Li , J. Luo , L. Wang , X. He , Int. J. Electrochem. Sci. 2011 , 6 , 1550 .

[32] Takeda, Y., Nakahara, K., Nishijima, M., Imanishi, N., Yamamoto, O., Takano, M., & Kanno, R. (1994). Sodium deintercalation from sodium iron oxide. *Materials Research Bulletin*, *29*(6), 659–666. doi: 10.1016/0025-5408(94)90122-8

[33] Zhang, L., Takada, K., Ohta, N., Osada, M., & Sasaki, T. (2007). Synthesis and electrochemistry of new layered (1−x)LiVO2·xLi2TiO3 (0≤x≤0.6) electrode materials. *Journal of Power Sources*, *174*(2), 1007–1011. doi: 10.1016/j.jpowsour.2007.06.082

[34] Asher, R. (1959). A lamellar compound of sodium and graphite. *Journal of Inorganic and Nuclear Chemistry*, *10*(3-4), 238–249. doi: 10.1016/0022-1902(59)80118-4

[35] Palacín, M. R. (2009). Recent advances in rechargeable battery materials: a chemist's perspective. *Chemical Society Reviews*, *38*(9), 2565. doi: 10.1039/b820555h
[36] Chevrier, V. L., & Ceder, G. (2011). Challenges for Na-ion Negative Electrodes. *Journal of The Electrochemical Society*, *158*(9). doi: 10.1149/1.3607983
[37] Ellis, L. D., Hatchard, T. D., & Obrovac, M. N. (2012). Reversible Insertion of Sodium in Tin. *Journal of The Electrochemical Society*, *159*(11). doi: 10.1149/2.037211jes
[38] Zhang, W.-J. (2011). A review of the electrochemical performance of alloy anodes for lithium-ion batteries. *Journal of Power Sources*, *196*(1), 13–24. doi: 10.1016/j.jpowsour.2010.07.020
[39] Armand, M., & Tarascon, J.-M. (2008). Building better batteries. *Nature*, *451*(7179), 652–657. doi: 10.1038/451652a
[40] Liu, Y. , Zhang, N. , Jiao, L. , Tao, Z. and Chen, J. (2015), Ultrasmall Sn Nanoparticles Embedded in Carbon as High-Performance Anode for Sodium-Ion Batteries. Adv. Funct. Mater., 25: 214-220. doi:10.1002/adfm.201402943
[41] Baggetto, L., Keum, J. K., Browning, J. F., & Veith, G. M. (2013). Germanium as negative electrode material for sodium-ion batteries. *Electrochemistry Communications*, *34*, 41–44. doi: 10.1016/j.elecom.2013.05.025
[42] Yabuuchi, N. , Matsuura, Y. , Ishikawa, T. , Kuze, S. , Son, J. , Cui, Y. , Oji, H. and Komaba, S. (2014), Phosphorus Electrodes in Sodium Cells: Small Volume Expansion by Sodiation and the Surface-Stabilization Mechanism in Aprotic Solvent. CHEMELECTROCHEM, 1: 580-589. doi:10.1002/celc.201300149
[43] Qian, J., Chen, Y., Wu, L., Cao, Y., Ai, X., & Yang, H. (2012). High capacity Na-storage and superior cyclability of nanocomposite Sb/C anode for Na-ion batteries. *Chemical Communications*, *48*(56), 7070. doi: 10.1039/c2cc32730a
[44] Stevens, D. A., & Dahn, J. R. (2001). The Mechanisms of Lithium and Sodium Insertion in Carbon Materials. *Journal of The Electrochemical Society*, *148*(8). doi: 10.1149/1.1379565
[45] Thomas, P., & Billaud, D. (2001). Sodium electrochemical insertion mechanisms in various carbon fibres. *Electrochimica Acta*, *46*(22), 3359–3366. doi: 10.1016/s0013-4686(01)00536-9
[46] Alcántara R., Mateos J. M. Jiménez, & Tirado, J. L. (2002). Negative Electrodes for Lithium- and Sodium-Ion Batteries Obtained by Heat-Treatment of Petroleum Cokes below 1000°C. *Journal of The Electrochemical Society*, *149*(2). doi: 10.1149/1.1431963
[47] Thomas, P., & Billaud, D. (2002). Electrochemical insertion of sodium into hard carbons. *Electrochimica Acta*, *47*(20), 3303–3307. doi: 10.1016/s0013-4686(02)00250-5
[48] Alcántara Ricardo, Lavela, P., Ortiz, G. F., & Tirado José L. (2005). Carbon Microspheres Obtained from Resorcinol-Formaldehyde as High-Capacity Electrodes for Sodium-Ion Batteries. *Electrochemical and Solid-State Letters*, *8*(4). doi: 10.1149/1.1870612
[49] Xia, X., Obrovac, M. N., & Dahn, J. R. (2011). Comparison of the Reactivity of NaxC6 and LixC6 with Non-Aqueous Solvents and Electrolytes. *Electrochemical and Solid-State Letters*, *14*(9). doi: 10.1149/1.3606364

[50] Komaba, S. , Murata, W. , Ishikawa, T. , Yabuuchi, N. , Ozeki, T. , Nakayama, T. , Ogata, A. , Gotoh, K. and Fujiwara, K. (2011), Electrochemical Na Insertion and Solid Electrolyte Interphase for Hard-Carbon Electrodes and Application to Na-Ion Batteries. Adv. Funct. Mater., 21: 3859-3867. doi:10.1002/adfm.201100854

[51] Barker, J., Gover, R. K. B., Burns, P., & Bryan, A. J. (2006). Hybrid-Ion. *Electrochemical and Solid-State Letters*, *9*(4). doi: 10.1149/1.2168288

[52] Wenzel, S., Hara, T., Janek, J., & Adelhelm, P. (2011). Room-temperature sodium-ion batteries: Improving the rate capability of carbon anode materials by templating strategies. *Energy & Environmental Science*, *4*(9), 3342. doi: 10.1039/c1ee01744f

[53] Liu, Y., Merinov, B. V., & Goddard, W. A. (2016). Origin of low sodium capacity in graphite and generally weak substrate binding of Na and Mg among alkali and alkaline earth metals. *Proceedings of the National Academy of Sciences*, *113*(14), 3735–3739. doi: 10.1073/pnas.1602473113

[54] Jeong, G., Kim, Y.-U., Kim, H., Kim, Y.-J., & Sohn, H.-J. (2011). Prospective materials and applications for Li secondary batteries. *Energy & Environmental Science*, *4*(6), 1986. doi: 10.1039/c0ee00831a

[55] Li, H. (1999). A High Capacity Nano-Si Composite Anode Material for Lithium Rechargeable Batteries. *Electrochemical and Solid-State Letters*, *2*(11), 547. doi: 10.1149/1.1390899

[56] Beaulieu, L. Y., Hewitt, K. C., Turner, R. L., Bonakdarpour, A., Abdo, A. A., Christensen, L., … Dahn, J. R. (2003). The Electrochemical Reaction of Li with Amorphous Si-Sn Alloys. *Journal of The Electrochemical Society*, *150*(2). doi: 10.1149/1.1530151

[57] Kim, H., Jeong, G., Kim, Y.-U., Kim, J.-H., Park, C.-M., & Sohn, H.-J. (2013). Metallic anodes for next generation secondary batteries. *Chemical Society Reviews*, *42*(23), 9011. doi: 10.1039/c3cs60177c

[58] Li, Z., Ding, J., & Mitlin, D. (2015). Tin and Tin Compounds for Sodium Ion Battery Anodes: Phase Transformations and Performance. *Accounts of Chemical Research*, *48*(6), 1657–1665. doi: 10.1021/acs.accounts.5b00114

[59] Wang, J. W., Liu, X. H., Mao, S. X., & Huang, J. Y. (2012). Microstructural Evolution of Tin Nanoparticles during In Situ Sodium Insertion and Extraction. *Nano Letters*, *12*(11), 5897–5902. doi: 10.1021/nl303305c

[60] Kim, Y., Kim, Y., Choi, A., Woo, S., Mok, D., Choi, N.-S., … Lee, K. T. (2014). Tin Phosphide as a Promising Anode Material for Na-Ion Batteries. *Advanced Materials*, *26*(24), 4139–4144. doi: 10.1002/adma.201305638

[61] Qian, J., Xiong, Y., Cao, Y., Ai, X., & Yang, H. (2014). Synergistic Na-Storage Reactions in Sn4P3 as a High-Capacity, Cycle-stable Anode of Na-Ion Batteries. *Nano Letters*, *14*(4), 1865–1869. doi: 10.1021/nl404637q

[62] Li, W., Chou, S.-L., Wang, J.-Z., Kim, J. H., Liu, H.-K., & Dou, S.-X. (2014). Sn4 xP3@ Amorphous Sn-P Composites as Anodes for Sodium-Ion Batteries with Low Cost, High Capacity, Long Life, and Superior Rate Capability. *Advanced Materials*, *26*(24), 4037–4042. doi: 10.1002/adma.201400794

[63] Ceder, G., Doyle, M., Arora, P., & Fuentes, Y. (2002). Computational Modeling and Simulation for Rechargeable Batteries. *MRS Bulletin*, *27*(8), 619–623. doi: 10.1557/mrs2002.198

[64] Bennion, D. N. (1976). Mathematical Model of a Lithium-Water Electrochemical Power Cell. *Journal of The Electrochemical Society*, *123*(10), 1462. doi: 10.1149/1.2132620

[65] W. Tiedemann and J. Newman, in *Battery Design and Optimization*, S. Gross, Editor, PV 79-1, p. 23, The Electrochemical Society Proceedings Series, Pennington, NJ (1979)

[66] P. Mukherjee, S. Pannala, and J. Turner, "Modeling and simulation of battery systems," *Handbook of Battery Materials, Second Edition*, pp. 841, (2011).

[67] Doyle, M. (1993). Modeling of Galvanostatic Charge and Discharge of the Lithium/Polymer/Insertion Cell. *Journal of The Electrochemical Society*, *140*(6), 1526. doi: 10.1149/1.2221597

[68] Fuller, T. F. (1994). Simulation and Optimization of the Dual Lithium Ion Insertion Cell. *Journal of The Electrochemical Society*, *141*(1), 1. doi: 10.1149/1.2054684

[69] Santhanagopalan, S., Guo, Q., Ramadass, P., & White, R. E. (2006). Review of models for predicting the cycling performance of lithium ion batteries. *Journal of Power Sources*, *156*(2), 620–628. doi: 10.1016/j.jpowsour.2005.05.070

[70] Haran, B. S., Popov, B. N., & White, R. E. (1998). Determination of the hydrogen diffusion coefficient in metal hydrides by impedance spectroscopy. *Journal of Power Sources*, *75*(1), 56–63. doi: 10.1016/s0378-7753(98)00092-5

[71] Q. Guo, R.E. White, private communication.

[72] Guo, M., Sikha, G., & White, R. E. (2011). Single-Particle Model for a Lithium-Ion Cell: Thermal Behavior. *Journal of The Electrochemical Society*, *158*(2). doi: 10.1149/1.3521314

[73] Chandrasekaran, R., Magasinski, A., Yushin, G., & Fuller, T. F. (2010). Analysis of Lithium Insertion/Deinsertion in a Silicon Electrode Particle at Room Temperature. *Journal of The Electrochemical Society*, *157*(10). doi: 10.1149/1.3474225

[74] Obrovac, M. N., Christensen, L., Le, D. B., & Dahn, J. R. (2007). Alloy Design for Lithium-Ion Battery Anodes. *Journal of The Electrochemical Society*, *154*(9). doi: 10.1149/1.2752985

[75] Chen, J. (2013). Recent Progress in Advanced Materials for Lithium Ion Batteries. *Materials*, *6*(1), 156–183. doi: 10.3390/ma6010156

[76] Xu, B., Qian, D., Wang, Z., & Meng, Y. S. (2013). Recent Progress in Cathode Materials Research for Advanced Lithium Ion Batteries. *ChemInform*, *44*(12). doi: 10.1002/chin.201312211

[77] Woodford, W. H., Carter, W. C., & Chiang, Y.-M. (2012). Design criteria for electrochemical shock resistant battery electrodes. *Energy & Environmental Science*, *5*(7), 8014. doi: 10.1039/c2ee21874g

[78] Pinson, M. B., & Bazant, M. Z. (2012). Theory of SEI Formation in Rechargeable Batteries: Capacity Fade, Accelerated Aging and Lifetime Prediction. *Journal of The Electrochemical Society*, *160*(2). doi: 10.1149/2.044302jes

[79] Ghassemi, H., Au, M., Chen, N., Heiden, P. A., & Yassar, R. S. (2011). In Situ Electrochemical Lithiation/Delithiation Observation of Individual Amorphous Si Nanorods. *ACS Nano*, *5*(10), 7805–7811. doi: 10.1021/nn2029814

[80] Liu, X. H., Zhong, L., Huang, S., Mao, S. X., Zhu, T., & Huang, J. Y. (2012). Size-Dependent Fracture of Silicon Nanoparticles During Lithiation. *ACS Nano*, *6*(2), 1522–1531. doi: 10.1021/nn204476h

[81] Lee, S. W., Mcdowell, M. T., Berla, L. A., Nix, W. D., & Cui, Y. (2012). Fracture of crystalline silicon nanopillars during electrochemical lithium insertion. *Proceedings of the National Academy of Sciences*, *109*(11), 4080–4085. doi: 10.1073/pnas.1201088109

[82] Lee, S. W., Ryu, I., Nix, W. D., & Cui, Y. (2015). Fracture of crystalline germanium during electrochemical lithium insertion. *Extreme Mechanics Letters*, *2*, 15–19. doi: 10.1016/j.eml.2015.01.009

[83] Ebner, M., Marone, F., Stampanoni, M., & Wood, V. (2013). Visualization and Quantification of Electrochemical and Mechanical Degradation in Li Ion Batteries. *Science*, *342*(6159), 716–720. doi: 10.1126/science.1241882

[84] Liang, W., Yang, H., Fan, F., Liu, Y., Liu, X. H., Huang, J. Y., … Zhang, S. (2013). Tough Germanium Nanoparticles under Electrochemical Cycling. *ACS Nano*, *7*(4), 3427–3433. doi: 10.1021/nn400330h

[85] Wang, J., Fan, F., Liu, Y., Jungjohann, K. L., Lee, S. W., Mao, S. X., … Zhu, T. (2014). Structural Evolution and Pulverization of Tin Nanoparticles during Lithiation-Delithiation Cycling. *Journal of The Electrochemical Society*, *161*(11). doi: 10.1149/2.0041411jes

[86] Koleshko, V. M., & Kiryushin, I. V. (1988). Deformation mechanism maps and gettering diagrams for single-crystal silicon. *Physica Status Solidi (a)*, *109*(1), 161–169. doi: 10.1002/pssa.2211090116

[87] Shi, X. Q., Wang, Z. P., Yang, Q. J., & Pang, H. L. J. (2002). Creep Behavior and Deformation Mechanism Map of Sn-Pb Eutectic Solder Alloy. *Journal of Engineering Materials and Technology*, *125*(1), 81–88. doi: 10.1115/1.1525254

[88] Barai, P., Huang, B., Dillon, S. J., & Mukherjee, P. P. (2016). Mechano-Electrochemical Interaction Gives Rise to Strain Relaxation in Sn Electrodes. *Journal of The Electrochemical Society*, *163*(14). doi: 10.1149/2.0801614jes

[89] Ning, G., & Popov, B. N. (2004). Cycle Life Modeling of Lithium-Ion Batteries. *Journal of The Electrochemical Society*, *151*(10). doi: 10.1149/1.1787631

[90] Garrick, T. R., Kanneganti, K., Huang, X., & Weidner, J. W. (2014). Modeling Volume Change due to Intercalation into Porous Electrodes. *Journal of The Electrochemical Society*, *161*(8). doi: 10.1149/2.030408jes

[91] Gomadam, P. M., & Weidner, J. W. (2006). Modeling Volume Changes in Porous Electrodes. *Journal of The Electrochemical Society*, *153*(1). doi: 10.1149/1.2136087

[92] Corless, R. M., Gonnet, G. H., Hare, D. E. G., Jeffrey, D. J., & Knuth, D. E. (1996). On the LambertW function. *Advances in Computational Mathematics*, *5*(1), 329–359. doi: 10.1007/bf02124750

[93] Abramowitz, M., & Stegun, I. A. (1965). *Handbook of mathematical functions: with formulas, graphs, and mathematical tables*. Washington: National Bureau of Standards.

[94] Jung, S. C., Choi, J.-H., & Han, Y.-K. (2018). The origin of excellent rate and cycle performance of Sn4P3 binary electrodes for sodium-ion batteries. *Journal of Materials Chemistry A*, *6*(4), 1772–1779. doi: 10.1039/c7ta07310k

[95] Chou, C.-Y., Lee, M., & Hwang, G. S. (2015). A Comparative First-Principles Study on Sodiation of Silicon, Germanium, and Tin for Sodium-Ion Batteries. *The Journal of Physical Chemistry C*, *119*(27), 14843–14850. doi: 10.1021/acs.jpcc.5b01099

[96] Olofsson, O., Aava, U., Haaland, A., Resser, D., Rasmussen, S. E., Sunde, E., & Sørensen, N. A. (1970). X-Ray Investigations of the Tin-Phosphorus System. *Acta Chemica Scandinavica*, *24*, 1153–1162. doi: 10.3891/acta.chem.scand.24-1153

[97] Lan, D., Wang, W., Shi, L., Huang, Y., Hu, L., & Li, Q. (2017). Phase pure Sn4P3 nanotops by solution-liquid-solid growth for anode application in sodium ion batteries. *Journal of Materials Chemistry A*, *5*(12), 5791–5796. doi: 10.1039/c6ta10685d

[98] Carboxymethyl Cellulose (CMC) for Li-ion Battery Anode 100g/bag - EQ-Lib-CMC. (n.d.). Retrieved from https://www.mtixtl.com/CarboxymethylCelluloseCMCbinderforLi-ionBatteryAnode100g/bottle.aspx.

[99] TIMCAL Graphite & Carbon Super P® Conductive Carbon Black, 100g/bag - EQ-Lib-SuperP. (n.d.). Retrieved from https://www.mtixtl.com/TIMCALGraphiteandCarbonSuperPConductiveCarbonBlack100g/bag-EQ-Li.aspx.

[100] Carbon Black(1333-86-4). (n.d.). Retrieved from https://www.chemicalbook.com/ProductMSDSDetailCB3109508_EN.htm.

[101] Thinky Corporation, & Morgan Advanced Materials - Technical Ceramics. (2019, October 16). Properties: An Introduction to Tin. Retrieved from https://www.azom.com/properties.aspx?ArticleID=615.

[102] Barai, P., & Mukherjee, P. P. (2016). Mechano-Electrochemical Stochastics in High-Capacity Electrodes for Energy Storage. *Journal of The Electrochemical Society*, *163*(6). doi: 10.1149/2.01191606jes

[103] Miller, D. J., Proff, C., Wen, J. G., Abraham, D. P., & Bareño, J. (2013). Observation of Microstructural Evolution in Li Battery Cathode Oxide Particles by In Situ Electron Microscopy. *Advanced Energy Materials*, *3*(8), 1098–1103. doi: 10.1002/aenm.201300015

[104] Higa, K., & Srinivasan, V. (2015). Stress and Strain in Silicon Electrode Models. *Journal of The Electrochemical Society*, *162*(6). doi: 10.1149/2.0091507jes

[105] Qi, Y., Hector, L. G., James, C., & Kim, K. J. (2014). Lithium Concentration Dependent Elastic Properties of Battery Electrode Materials from First Principles Calculations. *Journal of The Electrochemical Society*, *161*(11). doi: 10.1149/2.0031411jes

[106] Chen, L., Fan, F., Hong, L., Chen, J., Ji, Y. Z., Zhang, S. L., … Chen, L. Q. (2014). A Phase-Field Model Coupled with Large Elasto-Plastic Deformation: Application to Lithiated Silicon Electrodes. *Journal of The Electrochemical Society*, *161*(11). doi: 10.1149/2.0171411jes

[107] Wang, F., Yu, H.-C., Chen, M.-H., Wu, L., Pereira, N., Thornton, K., … Graetz, J. (2012). Tracking lithium transport and electrochemical reactions in nanoparticles. *Nature Communications*, *3*(1). doi: 10.1038/ncomms2185

[108] Zhang, X., Shyy, W., & Sastry, A. M. (2007). Numerical Simulation of Intercalation-Induced Stress in Li-Ion Battery Electrode Particles. *Journal of The Electrochemical Society*, *154*(10). doi: 10.1149/1.2759840